Journal of *Marine Science and Engineering*

MDPI

Article

Natural Convection Induced by Diurnal Heating and Cooling over a Fully Vegetated Slope

Xiaosheng Ji [1], Yi-Qi Ye [2], Bo Wang [1,*] and Ying-Tien Lin [2,3,*]

[1] Cryogenic Center, Zhejiang University City College, Hangzhou 310015, China; jixiaoshen@zju.edu.cn
[2] Institute of Port, Coastal and Offshore Engineering, Ocean College, Zhejiang University, Zhoushan 316021, China; 22034168@zju.edu.cn
[3] Engineering Research Center of Oceanic Sensing Technology and Equipment, Zhejiang University, Ministry of Education, Zhoushan 316021, China
* Correspondence: wangbo@zucc.edu.cn (B.W.); kevinlin@zju.edu.cn (Y.-T.L.)

Abstract: In this study, by assuming a small bottom slope, asymptotic solutions were developed to discuss natural convection within rooted emergent vegetation in response to different heating and cooling mechanisms. Based upon the maximum water depth in comparison to the penetration depth of solar radiation, two scenarios in shallow and deep waters were examined. The temperature structures showed that isotherms in shallows are near vertical but become stable stratified layers (horizontal isotherms) in deep regions. In shallow regions, horizontal velocity profiles perform classic cubic shapes, while the horizontal velocity in deep regions is constant near the surface, and a local upslope flow occurs near the bottom. In shallow water, viscous effects are dominant to shape the velocity profiles, whereas vegetation drag becomes more important in deep regions. By using turbulent parameters, horizontal exchange flowrates and velocities predicted by the asymptotic solutions show good agreements with the existing measurements.

Keywords: natural convection; rooted emergent vegetation; sloping bottom; diurnal heating and cooling; asymptotic solutions

Citation: Ji, X.; Ye, Y.-Q.; Wang, B.; Lin, Y.-T. Natural Convection Induced by Diurnal Heating and Cooling over a Fully Vegetated Slope. *J. Mar. Sci. Eng.* **2022**, *10*, 552. https://doi.org/10.3390/jmse10040552

Academic Editors: Dan Tchernov, Shin-Jye Liang and Tso-Ren Wu

Received: 12 March 2022
Accepted: 10 April 2022
Published: 18 April 2022

1. Introduction

In nearshore regions, natural convection (also called thermally driven flow) plays an important role in horizontal transport of nutrients, pollutants, or chemical substances in the absence of wind or other momentum forcing [1–5]. During the daytime, solar radiation penetrates into the water column and decays exponentially with water depths as Beer's law states [6]. The rate of decay is a function of the wavelength of the light and the turbidity of the water [7]. The absorbed solar radiation is then converted to heat, leading to warmer surface water than the underlying water. Temperature thus vertically varies along the water column, i.e., so-called stratification. Near the shore, sloping topography and profound vegetation both have significant impacts on the profiles of water temperature. For example, given the same amount of incident solar radiation into the water, during the daytime, shallower water absorbs more heat per unit volume than the adjacent deeper regions, leading to averagely warmer water in shallows than in deep regions [8]. The temperature differences result in variations of water density that cause convective flows developed toward offshore along the water surface and onshore near the bottom [9]. During the nighttime, the circulation is in the opposite direction to that during the daytime. On the other hand, floating and emergent vegetation can reduce a certain amount of incident sunlight into the water body, causing colder water in densely vegetated areas during the daytime [9,10]. The heterogeneous water temperature produced by vegetation shading can then drive exchange flows. Unlike floating vegetation, rooted emergent vegetation also provides inherent drag forces to slow down the circulation [7,8]. Due to diurnal heating and cooling processes, the induced natural convection flushes back and forth over the littoral

zones, which can renew nearshore water and promote horizontal exchanges of nutrients, chemical substances, and pollutants [9,10]. Several studies investigated the mechanisms of natural convection over a topographic slope [9–14] or from vegetation shading on a flat bottom [7,11,15]. Nevertheless, studies discussing the combined effects of sloping bottom and rooted emergent vegetation on natural convection have been given little attention.

The magnitude of natural convection observed over a nearshore slope can be up to ~15 cm/s, and time lag exists between the reversal of circulation and pressure gradient up to seven hours [10,16]. To reveal the underlying physics of the induced circulation owing to a slope, two models regarding distributions of incident solar radiation over the water column are commonly adopted. References [9,14] used a highly idealized model that neglects exponential decaying of solar radiation in water and assumes that solar radiation is uniformly distributed over the local water depth. They analytically found that the time lag between buoyancy and horizontal velocity can be up to 12 h. In addition, the flow is dominated by viscosity in shallows, while it becomes inertia-dominated in deep water. On the other hand, a more physically realistic model that considers exponential decays of incident sunlight with water depths during the daytime is also adopted. Farrow and Patterson [17] only included vertical heat conduction to derive asymptotic solutions to describe natural convection during daytime heating. Previous studies have shown that over a small slope bottom, natural convection can be classified into three distinct flow regimes—conductive, transitional, and convective—depending on the Rayleigh number, a function of vertical temperature gradients [18,19]. Once the vertical temperature gradient exceeds some specific criteria [20], thermal instability will occur, which is an important mechanism in breaking the residual circulation and reversing flow in deep water [18]. Lei and Patterson [21] found that bottom heating from the residual solar radiation is critical to drive the circulation, and aquatic environments with smaller light extinction coefficients can generate larger flows. Lei and Patterson [21] and Badnarz et al. [22] both showed a time lag of flow responses to the switches between diurnal heating and cooling, consistent with the field observations and analytical derivations. Despite a solid understanding of diurnal natural convection gained in these research studies, the effects of aquatic vegetation commonly found in nearshore regions are usually neglected.

In nearshore regions, extensively present floating and emergent vegetation intercepts the incident sunlight and shades the water body. Furthermore, rooted emergent vegetation inherently provides drag force to reduce the circulation and volumetric horizontal exchange flowrates and increase flushing time [13,23,24]. Horsch and Stefan [13] examined the impact of vegetation drag on exchange flows between vegetated and open waters during nighttime cooling. Oldham and Sturm [23] applied the porous media flow theory to study the effect of vegetation drags on exchange flows over a slope during surface cooling processes. Tanino et al. [24] investigated effects of rooted vegetation on horizontal velocity profiles of exchange flows over a flat bottom. The propagating front of exchange flows within vegetation converts to a triangular shape instead of a classic profile under no vegetation conditions. Based upon the model proposed by [10] (exponential decay of solar radiation in water is neglected), Lin and Wu [25] included vegetation drag to derive streamline and horizontal velocity of exchange flow over a slowly varying slope. They revealed that vegetation drag can reduce the time lag between reversal of flow and prevailing temperature gradients. Furthermore, vegetation drag replaces inertia to become the dominant mechanism in deep waters to characterize the horizontal velocity profiles. Lin and Wu [26] also used a more realistic model, i.e., the exponential decays of sunlight along the water column during the day and heat losses through the water during the night, to consider the natural convection in non-uniform vegetation distributions. However, the most fundamental case, natural convection within uniformly distributed vegetation, is not discussed. The dominant physical mechanism to shape the circulation patterns within uniformly distributed vegetation is still not clear.

In this paper, different natures of daytime heating and nighttime cooling are adopted to discuss natural convection within uniformly distributed and rooted emergent vegetation

over a slope. The asymptotic solutions derived in [26] are used to perform the temperature, streamline, and horizontal velocity profiles and elucidate the spatial and temporal dominant mechanisms between viscosity, vegetation drag, and inertial terms. Flow patterns and magnitude of natural convection within uniformly rooted emergent vegetation at different locations are revealed. The asymptotic solutions used to estimate exchange flowrates and horizontal velocities are compared with several existing measurements.

2. Mathematical Formulations

In this study, we applied the results of [26] in non-uniform vegetation distribution to discuss the natural convection within uniform vegetation distribution. The description is therefore kept to a minimum here, and readers can refer to the previous publication for further details. The flow domain is set up over a slope with rooted emergent vegetation growth (Figure 1). The domain is assumed to be two-dimensional: the origin is at the tip, x' is the horizontal coordinate, and $z'(= -Sx')$ is the vertical coordinate and positive upward from the water surface, where S is the bottom slope. The vegetation distribution is assumed to vary only along the x' direction and be vertically uniform, i.e., numbers of vegetation leaves and sizes of vegetation stands that change along the water column are neglected.

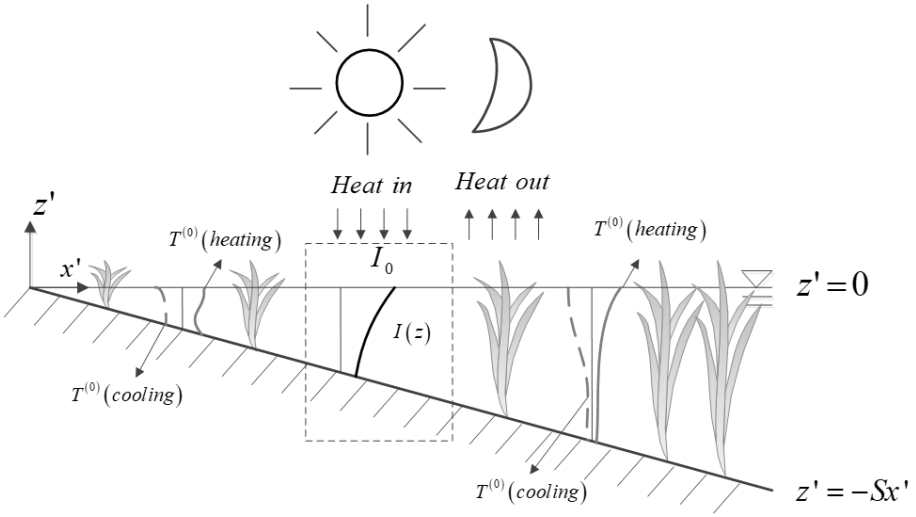

Figure 1. Geometry of the flow domain showing the coordinate system and different heating and cooling mechanisms.

Daytime heating and nighttime cooling are described as different forcing mechanisms. During the heating period, an internal heating source term Q'_{heat} is adopted in the energy equation to represent the solar radiation that enters the water column. The bulk solar radiation I is modeled by taking a periodic heat flux, and its intensity attenuates exponentially with the depth according to Beer's law, which is:

$$I = I_0 \cos(2\pi t'/\tau) e^{\eta z'}, \quad (1)$$

where I_0 is the heat flux of bulk solar radiation at the water surface, τ is the forcing period (24 h), η is the extinction coefficient, and $t' = 0$ is at noon. The extinction coefficient η is a function of the wavelength of the incident solar radiation and the turbidity of the water [13,21]. In this paper, we only consider the bulk behavior of the incoming radiation, and the turbidity is vertically uniform, which means that the extinction coefficient η can be represented as a single and constant value as previous studies assumed [7,13]. Equation (1) is applied for the heating period, i.e., $\cos(2\pi t'/\tau) \geq 0$. In the daytime, heat losses through the water surface are ignored, and all the solar radiation entering through the water surface is absorbed by the water body [20]. For the cooling period, i.e., $\cos(2\pi t'/\tau) < 0$, the heat source term is set to zero, i.e., $I_0 = 0$, and heat losses from the water surface.

Due to the presence of emergent vegetation, incident solar radiation into the water body will be reduced. Emergent vegetation with tall stands above the water surface can prevent more solar radiation from entering the water column than vegetation with short stands [15]. In the nighttime phase, emergent vegetation tends to reduce radiation losses, and water temperature in vegetated regions is higher than that in open regions [27]. In order to include the impact of vegetation shading, a reduction function $F(x')$ associated with vegetation distribution and height of vegetation stand is introduced. If emergent vegetation is uniformly distributed along the horizontal direction, emergent vegetation with tall and short stands leads to different reductions in solar radiation I_0 in the water, but the reduction is constant and less than unity, i.e., $F(x') =$ constant. The height of vegetation stands only decreases the magnitudes of heat gain and loss as well as circulation strength but not circulation patterns. The reduction function $F(x')$ can be estimated by in situ measurements. For instance, Lövstedt and Bengtsson [15] found that small amounts (~0.5%) of tall vegetation such as reeds (usually grow 2~3 m above the water surface) could block ~85% of incident solar radiation. Under this condition, $F(x')$ is equal to 0.15, i.e., 15% of incident solar radiation passing through vegetation stands.

The internal heat source term Q'_{heat} in the energy equation is given by:

$$Q'_{heat}(x', z', t') = \begin{cases} \frac{I_0 F(x') \eta e^{\eta z'} \cos(2\pi t'/\tau)}{\rho_0 C_p} \, (^\circ C/s), \cos(2\pi t'/\tau) \geq 0 \\ 0, \cos(2\pi t'/\tau) < 0 \end{cases}, \quad (2)$$

where ρ_0 is the reference density of water, and C_p is the specific heat of water.

Temperature differences are usually small in the nearshore regions, and the Boussinesq approximation on density variations can be adopted. The vegetation drag is assumed to act toward the horizontal direction and follows a quadratic drag law, i.e., $\frac{C_D a u'|u'|}{2}$ in the horizontal momentum equation [24], where u' is the horizontal velocity, C_D is the drag coefficient, and a is the frontal area of vegetation per unit volume.

For a two-dimensional flow, the governing equations are [10,28]:

$$\frac{\partial (n_v u')}{\partial x'} + \frac{\partial (n_v w')}{\partial z'} = 0, \quad (3)$$

$$n_v \left[\frac{\partial u'}{\partial t'} + u' \frac{\partial u'}{\partial x'} + w' \frac{\partial u'}{\partial z'} \right] = -\frac{n_v}{\rho_0} \frac{\partial P'}{\partial x'} - \frac{C_D a u'|u'|}{2} + n_v \nu \left(\frac{\partial^2 u'}{\partial x'^2} + \frac{\partial^2 u'}{\partial z'^2} \right), \quad (4)$$

$$n_v \left[\frac{\partial w'}{\partial t'} + u' \frac{\partial w'}{\partial x'} + w' \frac{\partial w'}{\partial z'} \right] = -\frac{n_v}{\rho_0} \frac{\partial P'}{\partial z'} + n_v \nu \left(\frac{\partial^2 w'}{\partial x'^2} + \frac{\partial^2 w'}{\partial z'^2} \right) + n_v g \alpha (T' - T_0), \quad (5)$$

$$n_v \left[\frac{\partial T'}{\partial t'} + u' \frac{\partial T'}{\partial x'} + w' \frac{\partial T'}{\partial z'} \right] = n_v \left[\kappa \left(\frac{\partial^2 T'}{\partial x'^2} + \frac{\partial^2 T'}{\partial z'^2} \right) + Q'_{heat}(x', z', t') \right], \quad (6)$$

where variables with a prime denote dimensional quantities, n_v is the porosity (the ratio of volume occupied by water to total volume), u' and w' are horizontal and vertical velocities, T' is temperature, P' is pressure, g is gravitational acceleration, α is the thermal expansion coefficient, ν is kinematic viscosity of water, and κ is the thermal diffusivity of water.

Under low stem Reynolds number Re_d ($=u'd/\nu$, where d is the stem diameter of vegetation), C_D is inversely proportional to $|u'|$, i.e., $\frac{2 n_v C}{|u'|}$ [24], where C is the linear drag coefficient. The vegetation drag can then be simplified as $C a u' n_v$ in Equation (4). According to data from [7], the relationship between the linear drag coefficient C and the solid volume fraction ϕ ($1 - n_v$, the ratio of vegetation volume to total volume in water) can be regressed as follows:

$$C = -0.3788\phi^2 + 0.1134\phi, \quad (7)$$

and the frontal area a for a cylindrical stem is given by:

$$a = \frac{4\phi}{\pi d} \quad (8)$$

The fluids are at rest and isothermal at $t' = 0$, and the thermal boundary conditions are according to the daytime heating or nighttime cooling phases. In the daytime phase, water surface is insulated, and the residual heat is absorbed by the bottom which is then immediately released as a bottom boundary heat flux. This bottom boundary condition ensures that the total heat at different water depths is conserved. For the nighttime period, heat releases through the water surface so that the bottom is assumed to be insulated. At the surface, it is shear-free, and no flow can occur across the surface. The bottom is impermeable, and the flow complies with the no-slip condition. The initial and boundary conditions are:

$$\begin{array}{l} T' = T_0, u' = w' = 0 \text{ at } t = 0; \\ \frac{\partial u'}{\partial z'} = 0 (\text{shear free}), w' = 0 \text{ on } z' = 0; \\ -k\frac{\partial T'}{\partial z'}(z' = 0) = \begin{cases} 0, \text{ for } \cos(2\pi t'/\tau) \geq 0, \\ -\frac{I_0 F(x')}{\rho_0 C_p}\cos(2\pi t'/\tau), \text{ for } \cos(2\pi t'/\tau) < 0, \end{cases} \text{ on } z' = 0; \\ u' = w' = 0 (\text{no slip}) \text{ on } z' = -Sx'. \end{array} , \quad (9)$$

$$-\kappa\frac{\partial T'}{\partial \hat{n}}(z' = -Sx') = \begin{cases} \frac{-\kappa}{\sqrt{1+S^2}}\left(S^2\frac{\partial T'}{\partial x'} + \frac{\partial T'}{\partial z'}\right) = \frac{I_0 F(x')}{\rho_0 C_p}e^{-\eta z'}\cos(2\pi t'/\tau), \text{ for } \cos(2\pi t'/\tau) \geq 0, \\ 0, \text{ for } \cos(2\pi t'/\tau) < 0, \end{cases}$$

where $\hat{n}$ is the direction normal to the sloping bottom, and T_0 is the reference temperature.

The following scales are used to non-dimensionalize the system of governing equations [9,16]:

$$t \sim \tau,\ z \sim H = \eta^{-1},\ x \sim H/S,\ T' - T_0 \sim \frac{I_0}{\rho_0 C_p}\eta\tau,\ P' \sim \rho g \alpha H_0 \tau,$$
$$u' \sim SGr\tau\eta^3\nu^2 \text{ and}$$
$$w' \sim S^2 Gr\tau\eta^3\nu^2$$

where the Grashof number Gr is given by:

$$Gr = \frac{g\alpha\Delta T H^3}{\nu^2} = \frac{g\alpha H_0 \tau}{\eta^2\nu^2} \quad (10)$$

The non-dimensional energy equation is given by:

$$\frac{\partial T}{\partial t} + S^2 Gr\tau^2\eta^4\nu^2\left(u\frac{\partial T}{\partial x} + w\frac{\partial T}{\partial z}\right) = S^2\eta^2\kappa\tau\frac{\partial^2 T}{\partial x^2} + \eta^2\kappa\tau\frac{\partial^2 T}{\partial z^2} + Q_{heat}(x, z, t), \quad (11)$$

where

$$Q_{heat}(x, z, t) = \begin{cases} F(x)e^z\cos(2\pi t)\text{, for} \cos(2\pi t) \geq 0 \\ 0, \text{ for } \cos(2\pi t) < 0 \end{cases}, \quad (12)$$

and variables T, t, x, z, u, and w are now dimensionless. By using stream function $\psi(u = -\frac{1}{n_v}\frac{\partial \psi}{\partial z}, w = \frac{1}{n_v}\frac{\partial \psi}{\partial x}$ [28]) and eliminating the pressure term, the dimensionless stream function equation is:

$$\begin{aligned} \psi_{tzz} + S^2\psi_{txx} + S^2 Gr\tau^2\eta^4\nu^2\tfrac{1}{n_v}[(\psi_x\psi_{zzz} \quad & -\psi_z\psi_{xzz}) + S^2(\psi_x\psi_{xxz} - \psi_z\psi_{xxx})] \\ & = \nu\eta^2\tau(\psi_{zzzz} + 2S^2\psi_{xxzz} + S^4\psi_{xxxx}) + S^2 Ca\tau\psi_{xx} - Ca\tau\psi_{zz} + n_v T_x \end{aligned} \quad (13)$$

The water surface and sloping bottom are along the same streamline, indicating that the streamline values are the same and set to zero for simplicity. The boundary conditions can be therefore shown as:

$$(1)\begin{cases} \psi = \psi_{zz} = 0, \\ \frac{\partial T}{\partial z} = 0 \text{ for } \cos(2\pi t) \geq 0, \\ \frac{\partial T}{\partial z} = F(x)\frac{\cos(2\pi t)}{\eta^2\kappa\tau} \text{ for } \cos(2\pi t) < 0, \end{cases} \text{ on } z = 0, \quad (14)$$

$$(2)\begin{cases} \psi = \psi_z = 0, \\ \frac{\partial T}{\partial n} = \frac{T_z + S^2 T_x}{\sqrt{1+S^2}} = -F(x)\frac{e^{-x}\cos(2\pi t)}{\eta^2 \kappa \tau} \text{ for } \cos(2\pi t) \geq 0, \text{on } z = -x \\ \frac{\partial T}{\partial n} = \frac{T_z + S^2 T_x}{\sqrt{1+S^2}} = 0 \text{ for } \cos(2\pi t) < 0, \end{cases} . \quad (15)$$

To analytically solve the governing equations, the piece-wise functions are used to represent the heat source term and boundary conditions (Equations (12), (14), and (15)). Fourier series is thus applied to expand the cosine function $\cos(2\pi t)$ from a half-period cycle ($0 \leq t \leq 0.5$ or $0.5 \leq t \leq 1$) to the whole-period cycle ($0 \leq t \leq 1$). The discrete heat source term and boundary conditions then become:

$$Q_{heat}(x,z,t) = F(x)\left\{\frac{1}{\pi} + \frac{\cos(2\pi t)}{2} + \sum_{m=2}^{\infty}\frac{2}{\pi}\left[\frac{\cos(m\pi/2)}{1-m^2}\right]\cos(2m\pi t)\right\}e^z, \quad (16)$$

$$\begin{cases} \psi = \psi_{zz} = 0, \\ \frac{\partial T}{\partial z} = -\frac{F(x)}{c_k}\left\{-\frac{1}{\pi} + \frac{\cos(2\pi t)}{2} - \sum_{m=2}^{\infty}\frac{2}{\pi}\left[\frac{\cos(m\pi/2)}{1-m^2}\right]\cos(2m\pi t)\right\} \text{ , on } z = 0, \end{cases} \quad (17)$$

$$\begin{cases} \psi = \psi_z = 0, \\ \frac{\partial T}{\partial z} = -F(x)\frac{I_{n\_0}}{I_{d\_0}}\frac{e^{-x}}{c_k}\left\{\frac{1}{\pi} + \frac{\cos(2\pi t)}{2} + \sum_{m=2}^{\infty}\frac{2}{\pi}\left[\frac{\cos(m\pi/2)}{1-m^2}\right]\cos(2m\pi t)\right\} \text{ , on } z = -x, \end{cases} \quad (18)$$

where $c_k = \eta^2 \kappa \tau$.

It is difficult to obtain the analytic solutions for Equations (11) and (13). Instead, the bottom slope S in typical field conditions is usually small, i.e., $S << 1$, which can be exploited to obtain asymptotic solutions for the dependent variables in Equations (11) and (13). Since the small slope S appears as even powers in Equations (11) and (13), the stream function ψ and temperature T can be expanded as a series of even power for S [10,25,29]:

$$\psi = \psi^{(0)} + S^2\psi^{(2)} + S^4\psi^{(4)} + \ldots, T = T^{(0)} + S^2 T^{(2)} + S^4 T^{(4)} + \ldots, \quad (19)$$

After substituting Equation (19) into Equations (11), (13), and (16) to (18) and equating the power of S, a system of equations with corresponding boundary conditions is yielded and can be solved recursively in principle. The zero-order (S^0) temperature is firstly solved, and in turn, the zero-order stream function equation can be solved according to the zero-order horizontal temperature gradient. The zero-order governing equations are:

$$T_t^{(0)} = c_k T_{zz}^{(0)} + F(x)\left\{\frac{1}{\pi} + \frac{\cos(2\pi t)}{2} + \sum_{m=2}^{\infty}\frac{2}{\pi}\left[\frac{\cos(m\pi/2)}{1-m^2}\right]\cos(2m\pi t)\right\}e^z, \quad (20)$$

$$\psi_{tzz}^{(0)} = c_v \psi_{zzzz}^{(0)} - c_d \psi_{zz}^{(0)} + n_v T_x^{(0)}, \quad (21)$$

where $c_k = \eta^2 \kappa \tau, c_v = \eta^2 \nu \tau, c_d = Ca\tau$.

With boundary conditions:

$$\begin{cases} \psi^{(0)} = {\psi_{zz}}^{(0)} = 0, \\ {T_z}^{(0)} = -\frac{F(x)}{c_k}\left\{-\frac{1}{\pi} + \frac{\cos(2\pi t)}{2} - \sum_{m=2}^{\infty}\frac{2}{\pi}\left[\frac{\cos(m\pi/2)}{1-m^2}\right]\cos(2m\pi t)\right\} \text{ , on } z = 0, \end{cases} \quad (22)$$

$$\begin{cases} \psi^{(0)} = {\psi_z}^{(0)} = 0, \\ T_z^{(0)} = -F(x)\frac{I_{n\_0}}{I_{d\_0}}\frac{e^{-x}}{c_k}\left\{\frac{1}{\pi} + \frac{\cos(2\pi t)}{2} + \sum_{m=2}^{\infty}\frac{2}{\pi}\left[\frac{\cos(m\pi/2)}{1-m^2}\right]\cos(2m\pi t)\right\} \text{ , on } z = -x, \end{cases} \quad (23)$$

The initial condition is:

$$\psi^{(0)} = T^{(0)} = 0, \text{ at } t = 0 \quad (24)$$

For typical field values, using $I_0 = 500$ W/m^2 and common values for the other parameters such as g, α, ρ, and C_p gives the Grashof number ranging from $Gr \approx 10^7$ for an eddy viscosity of $\nu = 10^{-4}$ m^{2}s^{-1} to $Gr \approx 10^9$ for the molecular viscosity ($\nu = 10^{-6}$ m^{2}s^{-1}) [14]. The bottom slope S usually varies from 10^{-2} to 10^{-3}. Therefore, S^2Gr is usually much larger (10~10^5). The asymptotic solution obtained in this study can be only applied to rare conditions such as very mild bottom slopes or very small incoming solar radiation. In addition, due to ignorance of the convective and horizontal conductive terms in Equation (11), the asymptotic solution can only fit the conductive flow regimes and lower transitional regions as [18] pointed out. Despite these limitations, the derived asymptotic solutions still show some interesting physical features and dynamics of the circulation.

The boundary value problem for zero-order temperature is linear, and each term in Equation (20) can be solved separately with corresponding boundary conditions, and then the full solutions are obtained from the solutions of each term superimposed. The solutions can be found by taking Laplace transform in t (see Appendix A). By taking derivative with respective to x, the temperature gradient $T_x^{(0)}$ that can be found is the forcing term in Equation (21). For uniform distributions of rooted emergent vegetation, i.e., $F(x) =$ contant, the terms associated with $\frac{dF}{dx}$ thus become zero, which will not contribute to $T_x^{(0)}$. The boundary value problems for $\psi^{(0)}$ are linear, and the forcing term $T_x^{(0)}$ can be solved separately. In turn, the full solution of $\psi^{(0)}$ can be obtained by superimposing the solutions of each term. The solution of each forcing term in $T_x^{(0)}$ (Appendix B) can be solved by using Laplace transform in t. The details of solving procedures can be referred to Farrow [29]. The full solutions for $\psi^{(0)}$ are provided in Appendix C. The zero-order horizontal velocity can be then obtained as: $u^{(0)} = -\frac{1}{n_v}\frac{\partial \psi^{(0)}}{\partial z}$.

3. Results and Discussions

3.1. Transient Behavior

Transient behavior of temperature $T^{(0)}$ and stream function $\psi^{(0)}$ can be examined by using e-folding time that causes the exponent term in $T^{(0)}$ and $\psi^{(0)}$ to decrease by a factor of e (Napier's constant). The e-folding times t_{e_T} and t_{e_ψ} of the transient terms of $T^{(0)}$ and $\psi^{(0)}$ are:

$$t_{e\_T} = \frac{1}{c_k}\left(\frac{x}{\pi}\right)^2, \tag{25}$$

$$t_{e\_\psi} = \frac{1}{c_v(\beta_1/x)^2 + c_d}, \tag{26}$$

where $\beta_1 \approx 4.49$. As [17] indicated, the e-folding times for $T^{(0)}$ and $\psi^{(0)}$ are indicative of the time elapse for heat and momentum to diffuse over the local water depth by thermal diffusivity and viscosity, respectively. As x becomes smaller, the e-folding time decreases. The flow at the region near the tip experiences shorter transient time and performs the periodic patterns (also called large-time behavior) more rapidly than that in the deep regions. Since temperature advection by flow motions is a second-order effect (Equation (20)), vegetation drag can reduce the circulation but is not related to the e-folding times t_{e_T} for $T^{(0)}$. In Equation (26), vegetation drag c_d is positive, which causes a smaller e-folding time t_{e_ψ} within vegetation than without vegetation, i.e., transient time within vegetation is shorter, which is the same as the case if temperature stratification is neglected [25].

The ratio of e-folding times t_{e_T} to t_{e_ψ} is:

$$\frac{t_{e\_T}}{t_{e\_\psi}} = \sigma\left(\frac{\beta_1}{\pi}\right)^2 + \frac{c_d}{c_k}\left(\frac{x}{\pi}\right)^2, \tag{27}$$

where σ is Prandtl number and approximately equal to 7 for water in laminar flow. Because $\sigma\left(\frac{\beta_1}{\pi}\right)^2$ is larger than 1, t_{e_T} is always longer than t_{e_ψ} both within and without the presence

of vegetation. Therefore, heat would diffuse to the entire water column more slowly than viscosity transporting momentum to the entire water column.

3.2. Temperature Profiles

The temperature profiles at shallow ($z \ll 1$) and deep ($z \ll 1$) waters are discussed within uniformly distributed vegetation, i.e., the shading function $F(x') = c =$ constant. The vegetation is assumed to grow very close to the water surface. The emergent vegetation reduces the incident sunlight into the water; meanwhile, vegetation stands decrease the volume occupied by water. For instance, vegetation with volumetric density ϕ = 0.25% (99.75% occupied by water) blocks 0.25% of incident sunlight, i.e., allowing 99.75% solar radiation impinging into 99.75% volume of water body. Therefore, the volumetric absorption of incident sunlight in the water body for 0.25% vegetation and no vegetation is the same. The constant c is then equal to 1, and the temperature magnitude and contours for 0.25% vegetation are the same as the case without vegetation. However, additional vegetation drag would slow down the flow field. In field situations, vegetation leaves typically have a larger area than the stand cross-sectional area, in which case the constant c may be less than 1.

In Equations (20) and (21), temperature and streamline profiles are related to the coefficient c_k, which is a function of η. In order to study temperature and streamline patterns, η needs to be first assigned. Herein, we choose η as 2, a common value found in typical field conditions, and in turn form two dimensionless water depths $z(=h\eta$, where h is the dimensional water depth) as 0.4 (shallow, h = 0.2 m) and 5 (deep, h = 2.5 m). For $z \ll 1$, i.e., the water depth h much less than the penetrating depth of solar radiation implies that a significant portion of the radiation can penetrate through the water column and reach the bottom. The residual heat is then reemitted from the bottom as a heat flux. For $z \ll 1$, i.e., the water depth greater than the penetration depth of the solar radiation, most of the solar radiation is absorbed in the top layer of the water column, and little solar radiation can penetrate through the water column and reach the bottom.

To make analytical progress, the non-linear terms such as thermal and flow convection need to be neglected, which excludes the effect of thermal instability and subsequent flow convection. Thermal instability usually originates at the free surface during nighttime cooling, and the fingers penetrate deep into the water column removing the stratification produced by sunlight [21]. As [21] pointed out, thermal instability can accelerate vertical mixing. Thus, to compensate for the ignorance of thermal and flow convection, the thermal diffusivity κ is manually increased to $1.4 \times 10^{-6}\left(\mathrm{m}^2/\mathrm{s}\right)$, ten times larger than the value in laminar flows. The increased thermal diffusivity promotes the vertical heat conduction and reduces the required time to remove the stratification. This can partially reflect the effects of thermal instability and flow convection.

The simulation begins at midday, i.e., $t = 0$ is at 12 p.m. (Figure 2). In the daytime ($t = 0.25$), less solar radiation in shallow waters is absorbed in the water column, and most of the solar radiation is reemitted as a bottom heat flux. For $z < 0.4$, vertical isotherms are revealed, i.e., temperature is vertically uniform showing unstratified patterns (Figure 2a). This can be explained by rapid heat diffusion and mixing over the entire water column for $z < 0.4$. A theoretical time scale t_{heat} for heat to diffuse over the entire water column is equal to $\frac{h^2}{\kappa}$ [16]. For this case, $z = 0.4$ and $\eta = 2$ mean the local water depth h of 0.2 m, yielding the time scale of 0.33 day. For $0.4 < z < 2.5$, heating from the bottom boundary is more important than that due to internal heating as [17,18] indicated. The warm and less dense fluid underlying cooler denser fluid is a potentially unstable source [17]. For $z > 2.5$, temperature is warmer near the water surface and colder near the bottom (Figure 2b). The internal heating component surpasses the bottom heating, and in fact, the bottom is effectively insulated [17]. Stable stratified layers (horizontal isotherms) are formed.

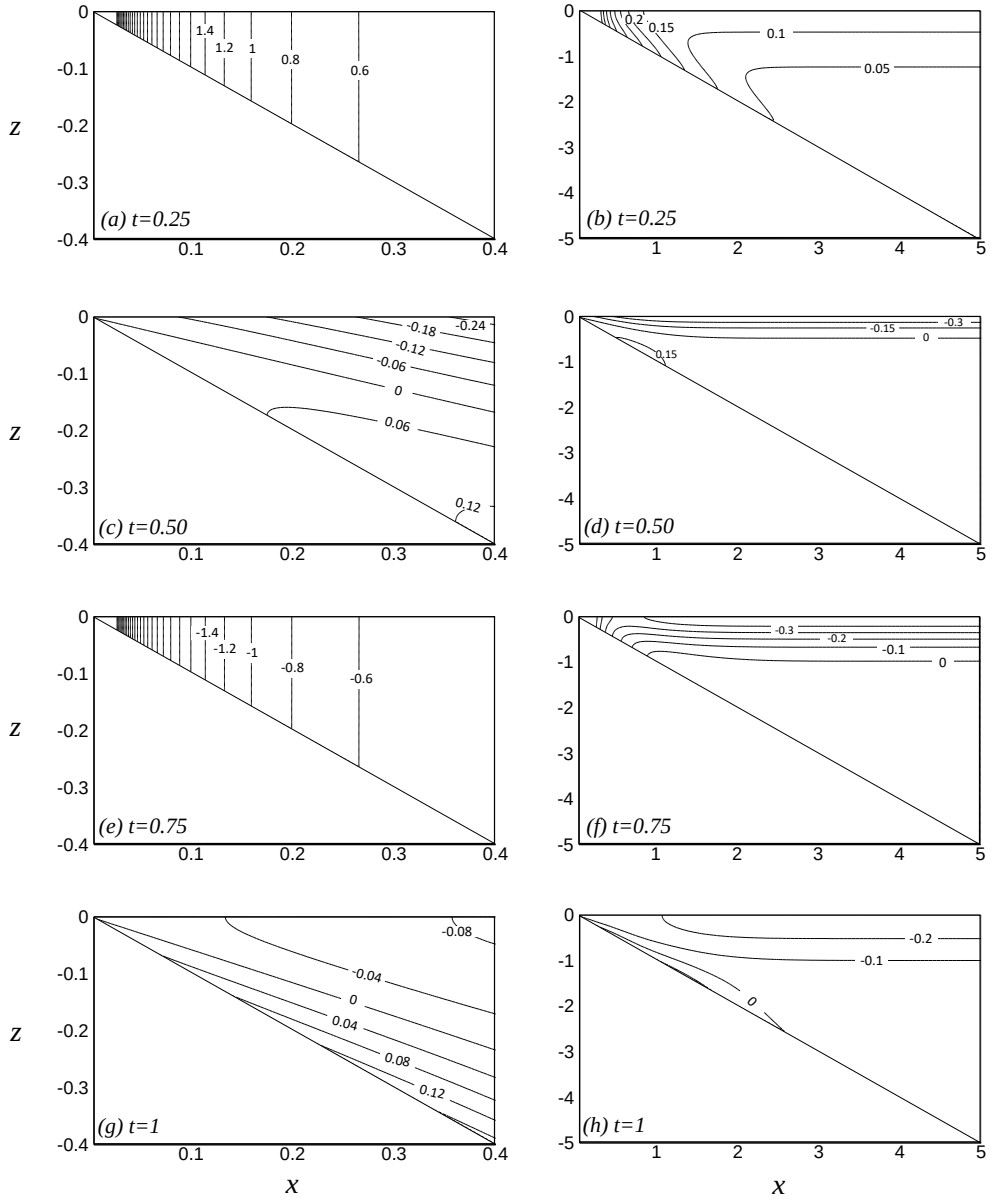

Figure 2. Temperature contours at z = 0.4 and 5 for various times. (**a**,**b**) t = 0.25, (**c**,**d**) t = 0.50, (**e**,**f**) t = 0.75, and (**g**,**h**) t = 1.

At $t = 0.25$, heat begins to dissipate through the water surface. Temperature at t = 0.50 is thus colder near the water surface and warmer near the bottom (Figure 2c,d). At $t = 0.75$, vertical isotherms (unstratified patterns) can be observed at the depth z less than 0.6, and horizontal isotherms are performed at deeper regions (Figure 2e,f). Once heating is switched on again (t = 1), bottom heating leads to warmer water along the sloping boundary until the depth z reaches 2.5 (Figure 2g,h). At deep water ($z > 2.5$), the solar radiation rises the water temperature near the surface (Figure 2h). Although the thermal diffusivity is manually increased, the unstable situations of warm water below cold water can sometimes still be found, which were also shown in numerical simulations [20], even though the thermal instability was taken into consideration. This is because the time is too short to overturn the underlying warmer water in the entire domain.

3.3. Horizontal Velocity Profiles

The horizontal velocities at three different vegetation densities at shallow ($z = 0.4$) and deep ($z = 2.5$) regions are shown in Figure 3. Emergent vegetation is uniformly distributed

along the horizontal and vertical directions with a volumetric vegetation density (ϕ) of 0.2% and a diameter of 0.6 cm, commonly found in typical field conditions. In shallows (Figure 3a), the flows show the classic cubic profile as [17,30] revealed. As the vegetation population becomes dense, the shape of the flows still holds, but the flow strength decreases. The nighttime flows ($t = 0.75$) are weaker than the daytime ones ($t = 0.25$) because during the nighttime, the reversed pressure gradients will develop until heat losses reach the sloping boundary. In the upper layer of deep waters, temperature contours show nearly horizontal isotherms, driving much less flow (Figure 3b). The curling of the isotherm near the bottom ($z = -x$) produces apparent horizontal temperature gradients and upslope flows as [31] mentioned. It is also noted that the pressure gradients induced by nighttime cooling are too weak to reverse the flow. Therefore, positive flows near the surface are still observed (Figure 3b). In addition, 0.2% vegetation only causes a slight reduction in horizontal velocity in shallows but results in significant decreases in flows in deep regions. This is associated with the dominant mechanics of induced flows at different depths. We discuss the phenomena in the next section.

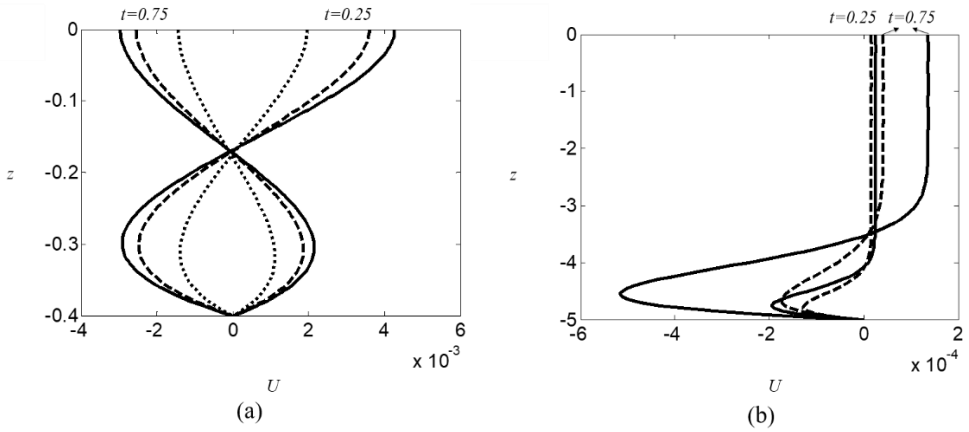

Figure 3. Comparisons of horizontal velocity profiles in (**a**) z = 0.4 and (**b**) z = 5 with different vegetation densities during daytime heating. ($\phi = 0\%$: ——, $\phi = 0.2\%$: – –, $\phi = 0.5\%$: ▪▪▪▪).

3.4. Dominant Physical Mechanisms

To discuss the dominant mechanism of natural convection at different water depths, the limiting cases that only keep one term among the terms $\psi^{(0)}_{tzz}$, $c_v\psi^{(0)}_{zzzz}$, and $c_d\psi^{(0)}_{zz}$ in Equation (21) to balance with the driving force T_x are derived and compared with the full solutions. For example, by balancing the inertial term with the driving force, i.e., $\psi^{(0)}_{tzz} = n_v T^{(0)}_x$ with the initial condition $t = 0$, $\psi = 0$ and boundary conditions $\psi = 0$ on $z = 0$ and $z = -x$, the solutions of inertial-limited streamlines and horizontal velocity can be obtained. Similarly, the horizontal velocity for pure drag or viscosity balance can be derived. The limiting cases of pure drag and inertia balances only use the boundary conditions of $\psi = 0$ on $z = 0$ and $z = -x$. The solutions for each limiting case are redundant and not provided here. References [10,14,25] used the thickness of the viscous boundary layer over one diurnal cycle to determine the region of the dominated mechanism. Since the viscous boundary layer thickness δ is equal to $\sqrt{\nu t}$, it grows to 0.29 m for a molecular viscosity of 10^{-6} m^{2}s^{-1} over one daily cycle (24 h). For a depth less than δ, viscosity is dominated to shape the horizontal velocity profiles. On the other hand, for a water depth larger than δ, the inertia is dominated in the absence of vegetation [10], whereas vegetation drag becomes more important if vegetation is present [25].

Figure 4 shows horizontal velocity profiles for the full (without and within vegetation) and pure viscous balance solutions at $z = 0.4$ ($\eta = 2$ and dimensional water depth h = 0.2 m). Since h is less than the viscous boundary layer thickness δ (=0.29 m), the horizontal velocity profiles obtained from the full solution (without vegetation) agree well with the predictions by a pure viscous/buoyancy balance at t = 0.25 and 0.75. The impact

of vegetation drag causes the differences between the full (within 0.2% vegetation) and pure viscous/buoyancy balance solutions. As water depth decreases, horizontal velocity profiles from the full solution and pure viscous/buoyancy balance become closer. Therefore, viscosity is the main dominant mechanism to determine horizontal velocity profiles in unvegetated and vegetated shallow waters as the cases when the stratified effects are ignored [10,25].

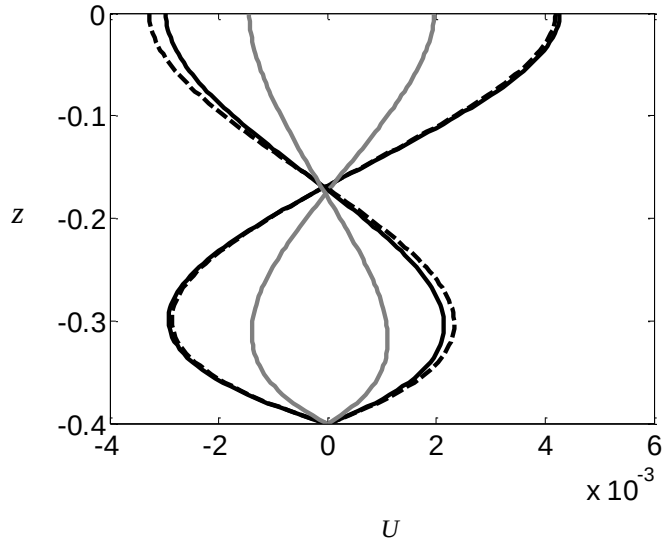

Figure 4. Horizontal velocity profiles in shallows at different times for the full solutions without vegetation (black solid) and with 0.2% vegetation (gray line) and pure viscosity balance (dashed line) solutions for z = 0.4.

The circulation is initially in an inertia/buoyancy balance, and viscosity progressively diffuses to the entire water column as time marches [7]. The time for viscosity diffusing to the entire water depth h is: $t_\nu = \frac{h^2}{\nu}$. At water depths h of 0.2 m ($z = 0.4$) and 2.5 m ($z = 5$) adopted in this study, t_ν is equal to 0.46 and 72.3 days accordingly. Figure 5 compares horizontal velocity profiles for the full and pure inertia/buoyancy balance solutions at $z = 0.4$. At $t = 0.001$, horizontal velocity profiles based on a pure inertia/buoyancy balance match well with the full solutions except for the region near the bottom, where viscosity prevails. The shape of horizontal velocity profiles at $z = 5$ is similar to those for $z = 0.4$, but the circulation magnitude and relevant time scales are different.

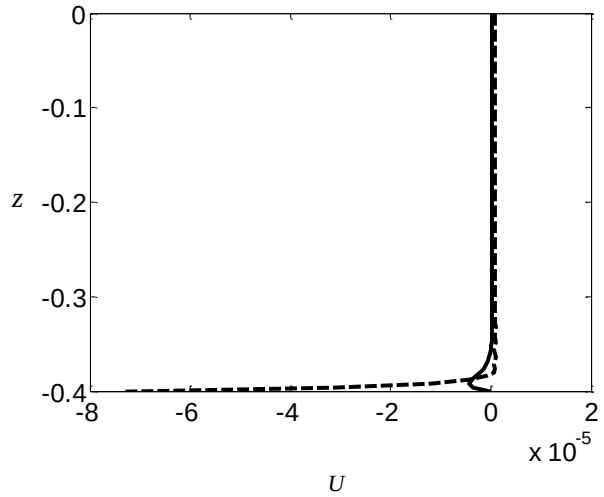

Figure 5. Horizontal velocity profiles for the full (solid line) and pure inertia balance (dashed line) solutions for z = 0.4 at t = 0.001.

Figure 6 presents horizontal velocity profiles for the full and pure drag/buoyancy balance solutions in deep regions ($z = 5$, and $h \approx 8.62\delta$). Horizontal velocity profiles obtained for the full and pure drag/buoyancy balance solutions are similar except for the region near the bottom where viscosity is important. Above $z = -4.5$, velocity is essentially like a plug profile and constant with depth. Below $z = -4.5$, a stronger uphill flow is found. The plug profile in the drag-dominated case is quite different from the velocity profiles in the unstratified case, where an inclined straight-line velocity profile is found in the drag-dominated range [25].

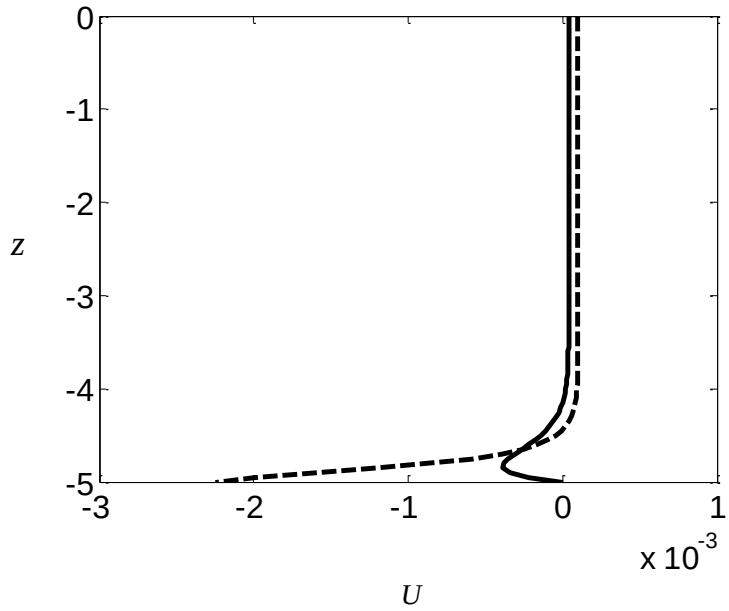

Figure 6. Horizontal velocity profiles for the full (solid line) and pure vegetative drag balance (dashed line) solutions at $t = 1.25$ and $z = 5$.

3.5. Flow Characteristics

Figure 7 shows contours of the surface velocity $u|_{z=0}$ in the (x,t) domain. As above-mentioned, the flow behavior is mainly controlled by viscosity and slightly reduced by vegetation drag in shallows. The plus (+) and minus (−) signs separated by the zero contour in Figure 7 indicate that the flow is out from the tip or into the tip of the domain, respectively. Here, we only perform the circulation patterns without vegetation because the vegetation mainly reduces the flow strength and does not change the flow patterns. For a small x ($x < 0.4$), the surface velocity changes the direction at $t = 0.5, 1, 1.5, 2, \ldots$, corresponding to the time instant when the direction of horizontal temperature gradients reverses (Figure 7). The time lag t_{lag} (time difference between the reversal of flow and horizontal pressure gradients) is zero, and the flow motions are in phase with the temperature gradients (also called phase lock). As x increases, time lag becomes more evident due to the decreasing viscous effect (Figure 7). For $x < 0.7$, positive and negative surface velocities alternatively appear during the daily cycle (Figure 7). As x increases, bottom heating in the daytime phase gradually controls the circulation, causing the appearance of positive flows more frequently than negative flows. When $x > 0.7$, the circulation will not reverse because the opposite pressure gradients from nighttime cooling are not strong enough to overcome the daytime pressure gradients. Furthermore, the flow strength is generally proportional to the water depth and reaches a peak at $x = 2$ as a result of decreasing viscous effects. For $x > 2$, the pressure gradients induced by temperature differences also decrease, and the flow intensity is thus reduced.

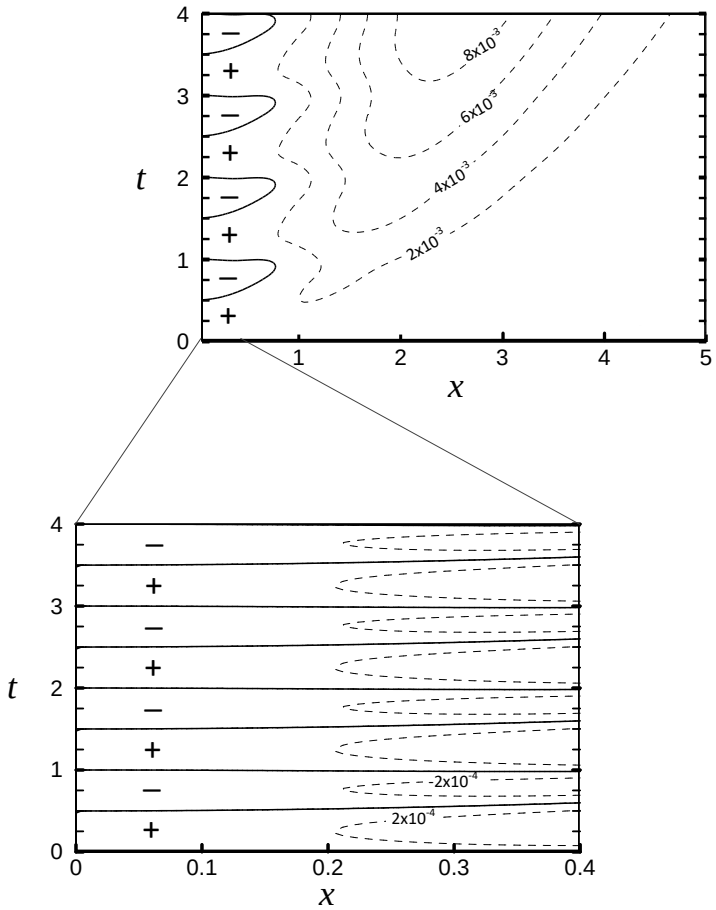

Figure 7. Contours of the surface velocity $u|_{z=0}$ in the (x,t)-plane after the forcing is initiated. The solid contour represents the zero contour, i.e., stagnation points.

3.6. Data Comparisons

The derived asymptotic solutions neglect the non-linear terms in the governing equations and can only be used in very rare field conditions. In order to expand the feasible range of the solutions, Reference [9] suggested using eddy viscosity ($\nu = 10^{-4}\mathrm{m}^2\ \mathrm{s}^{-1}$) instead of molecular viscosity ($\nu = 10^{-6}\mathrm{m}^2\ \mathrm{s}^{-1}$) to obtain reasonable estimates. Herein, eddy viscosity ($\nu = 10^{-4}\mathrm{m}^2\ \mathrm{s}^{-1}$), turbulent Prandtl number (=0.85, [31]), and turbulent thermal diffusivity ($\kappa = 1.18 \times 10^{-4}\mathrm{m}^2\ \mathrm{s}^{-1}$) are adopted. Horizontal velocity profiles from asymptotic solutions are compared with the experiments [23] conducted in a constructed wetland mesocosm during the nighttime with heat loss being approximately 100 Wm^{-2}. The mesocosm was vegetated with *Schoenoplectus validus* (diameter of 0.15 m and 16% volumetric density) in the shallow regions. The water velocity profiles were measured by using a Sontek 3D acoustic Doppler velocity (ADV) at the interface between open water and vegetation. The field data and asymptotic solutions shown in Figure 8 fall in a similar range and show the same trend that surface flows (approximately 1–2 mms^{-1}) were larger than bottom undercurrent velocities (approximately 0.5–1 mms^{-1}). The deviations between the prediction and measurements may be attributed to that (1) the mesocosm consists of two different slopes—a slope of 1:11 in the shallow regions and a slope of 1:3.5 in deep regions—and the averaged slope is used in comparisons, and that (2) the net fluxes at two measurement sections are not zero, violating the assumption of mass conservation adopted in our model.

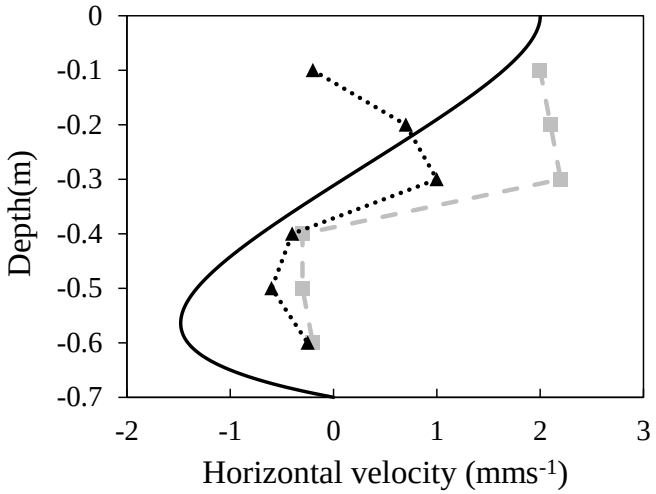

Figure 8. Comparisons of horizontal velocity profiles between the asymptotic solutions (solid lines) and data from [22] (dash and dot lines).

In addition, we compare horizontal exchange flowrates obtained in several field measurements [1,9,16,32] with theoretical predictions. The averaged dimensionless horizontal exchange flowrate (Q_{avg}) over a one-day cycle is calculated and given by [13]:

$$Q_{avg}(x,t) = \frac{1}{2}\int_{t}^{t+1}\int_{-x}^{0}|u(x,z,\tau)|dzd\tau, \tag{28}$$

For simplicity, we consider the averaged horizontal exchange flowrates Q_{avg} for the large time period. Table 1 shows relevant parameters from several previous measurements, in which water depths spanned from shallow (~1 m) to deep waters (~12 m). As above-mentioned, the turbulent parameters are used to estimate horizontal exchange flowrates. Comparisons between measurements and theoretical predictions are provided in Figure 9. The light extinction coefficients were usually not documented in these previous studies, and therefore the values commonly found in the field, i.e., $0.5 < \eta < 3$, were used in the calculation. In shallow waters, because of rapid heat mixing over the entire water column, the temperature is in fact vertically uniform, and the predicted exchange flowrates are the same for $\eta = 0.5$ to 3. The magnitude of horizontal exchange flowrates is generally proportional to the water depths. For the field measurements conducted by [9,16], horizontal exchange flowrates were obtained at the depths of 12 m (slope is 0.02 and 600 m away from the shore) and 8 m (slope is 0.007 and 1700 m away from the shore), respectively, where temperature exponentially decreases with the depth. A range of horizontal exchange flowrates derived from $\eta = 0.5$ to 3 is provided in which field measurements are covered. The asymptotic solutions can generally well predict the measurements at various scales. Horizontal exchange flowrates measured in open water and within submerged vegetation were also compared (see "◇" and "△" in Figure 9). Although our model is limited to emergent vegetation, estimated exchange flowrates for volumetric vegetation density between 0 to 1% can still match the measured exchange flowrates. The differences between the measurements and predictions may be primarily from the ignorance of three-dimensional topography in our two-dimensional model [30].

Table 1. Relevant parameters for field measurements.

Symbol	I_0 (W/m^2)	S	Depth (m)	Vegetation Type	Data Source
◇	500	0.0033	1	Submerged	[1]
△	500	0.0033	1	No	[1]
×	200	0.0175	1.8	No	[32]
○	400	0.02	8	No	[16]
□	500	0.007	12	No	[9]

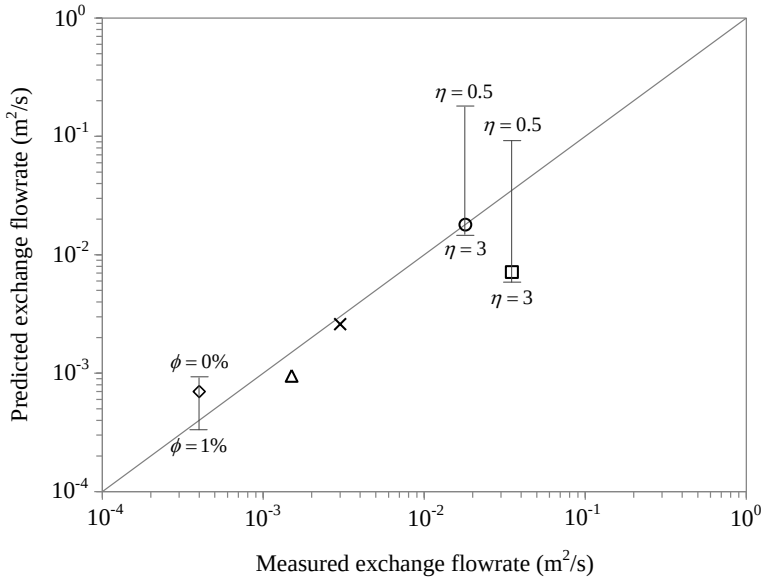

Figure 9. This is a figure. Schemes follow the same formatting. Comparisons of horizontal exchange flowrates between the prediction solution and measurements. "◇" and "△" are data from [1]; "×" is from [32]; "○" and "□" are from [16] and [9], respectively.

4. Conclusions

The study included the vegetation drag into the horizontal momentum equation and discussed natural convection in the presence of rooted and uniform emergent vegetation. The different heating and cooling mechanisms were taken into account in the asymptotic solutions. Based upon the maximum water depth in comparison to the penetration depth of solar radiation, two scenarios in shallow and deep waters, respectively, were examined. The temperature structures show that isotherms in shallows are near vertical but become horizontal layers in deep regions. In shallow regions, horizontal velocity profiles perform classic cubic shapes, while the horizontal velocity in deep regions is constant near the surface, and a local upslope flow occurs near the bottom. In shallow water, viscous effects are predominant, and the horizontal velocity can be represented as a pure viscosity/buoyancy balance. Without vegetation and in deep regions, horizontal velocity profiles from the full solution and a pure inertia/buoyancy balance are alike except for the regions near the bottom where viscosity prevails. On the other hand, within uniformly distributed vegetation, the horizontal velocity profiles in deep water can be characterized by a pure vegetation drag/buoyancy balance beside the near bottom regions.

This study used a conceptual and linear analytical model to investigate the effects of vegetation distributions on natural convection. The asymptotic solutions not only exclude the flow instability but also limit the density of the vegetation population. The results here perform more qualitative features rather than quantitative ones. Although the non-linear terms in the governing equations are ignored, the asymptotic solutions derived still show some interesting physical features and dynamics of the circulation. In addition, by using turbulent viscosity and thermal diffusivity, the asymptotic solutions are able to provide reasonable estimates of horizontal velocity and exchange flowrates in comparison with existing experimental data. The use of turbulent parameters expands the feasibility of the asymptotic solutions to typical field conditions. In general, although the analytical approach is old-fashioned and possibly unfeasible in many real conditions, it can be the first step to understand qualitative physical responses with certain limitation and provide references for field observations, laboratory tests, or numerical simulations. Furthermore, the analytical approach can clearly demonstrate the effects of different forcing such as inertia, viscosity, and vegetative drag on natural convection with various spatial and temporal scales. However, in order to understand physical phenomena in natural water

bodies, future works such as numerical modeling and field measurements are worthwhile and necessary.

Author Contributions: Conceptualization, X.J., B.W. and Y.-T.L.; Methodology, X.J. and Y.-T.L.; Data Analysis, Y.-Q.Y. and B.W.; Writing—Original Draft Preparation, Y.-T.L., Y.-Q.Y. and X.J.; Writing—Review and Editing, B.W.; Funding Acquisition, Y.-T.L. All authors have read and agreed to the published version of the manuscript.

Funding: This research was funded by the Zhejiang Provincial Natural Science Foundation of China (Grant No. LY20A020009).

Institutional Review Board Statement: Not applicable.

Informed Consent Statement: Not applicable.

Data Availability Statement: All data generated or analyzed during this study are included in this article.

Conflicts of Interest: The authors declare no conflict of interest.

Appendix A. Solutions of Zero-Order Temperature $T^{(0)}$

$$\begin{aligned}
T^{(0)} = \; & F(x)\left\{\frac{1}{c_k\pi}\left(\frac{1-e^{-x}}{x}-e^{z}\right)+\frac{\sin(2\pi t)}{2\pi x}+\frac{\cos(2\pi t)}{2c_k}\left[2\left(\frac{z^2}{2x}+z+\frac{x}{3}\right)+\left(\frac{1-e^{-x}}{x}-e^{z}\right)\right]\right. \\
& -\frac{2}{x\pi c_k}\sum_{n=1}^{\infty}\left\{\left[-\frac{1-(-1)^n e^{-x}}{1+(n\pi/x)^2}\right]\exp\left(-\frac{n^2\pi^2 c_k}{x^2}t\right)+\frac{\pi}{2}\left[\frac{2x^2}{n^2\pi^2}-\frac{1-(-1)^n e^{-x}}{1+(n\pi/x)^2}\right]\right. \\
& \left.\left.\times\left\{\exp\left(-\frac{n^2\pi^2 c_k}{x^2}t\right)-2\pi\left[\frac{2\pi\exp\left(-n^2\pi^2 c_k t/x^2\right)-2\pi\cos(2\pi t)+\left(n^2\pi^2 c_k/x^2\right)\sin(2\pi t)}{n^4\pi^4 {c_k}^2/x^4+4\pi^2}\right]\right\}\right\}\times\cos\frac{n\pi z}{x} \\
& +\sum_{m=2}^{\infty}\frac{2}{\pi}\left[\frac{\cos(m\pi/2)}{1-m^2}\right]\left\{\frac{\cos(2m\pi t)}{c_k}\left(\frac{1-e^{-x}}{x}-e^{z}\right)\right\} \\
& -\frac{4}{x\pi c_k}\sum_{m=2}^{\infty}\sum_{n=1}^{\infty}\left[\frac{\cos(m\pi/2)}{1-m^2}\right]\left[-\frac{1-(-1)^n e^{-x}}{1+(n\pi/x)^2}\right]\times\cos\frac{n\pi z}{x} \\
& \left.\times\left\{\exp\left(-\frac{n^2\pi^2 c_k}{x^2}t\right)-2m\pi\left[\frac{2m\pi\exp\left(-n^2\pi^2 c_k t/x^2\right)-2m\pi\cos(2m\pi t)+\left(n^2\pi^2 c_k/x^2\right)\sin(2m\pi t)}{n^4\pi^4 {c_k}^2/x^4+4m^2\pi^2}\right]\right\}\right\}
\end{aligned} \tag{A1}$$

Appendix B. Zero-Order Horizontal Temperature Gradients $T_x^{(0)}$

$$\begin{aligned}
T_x^{(0)} = \; & a_0(x)+b_0(x)\sin(2\pi t)+c_0(x)\cos(2\pi t)+d_0(x)z^2\cos(2\pi t) \\
& +\sum_{n=1}^{\infty}a_n(x)\sin(2\pi t)\cos(n\pi z/x)+\sum_{n=1}^{\infty}b_n(x)\cos(2\pi t)\cos(n\pi z/x)+\sum_{n=1}^{\infty}c_n(x)z\sin(2\pi t)\sin(n\pi z/x) \\
& +\sum_{n=1}^{\infty}d_n(x)z\cos(2\pi t)\sin(n\pi z/x)+\sum_{n=1}^{\infty}e_n(x)\exp\left(-n^2\pi^2\sigma t/x^2\right)\cos(n\pi z/x)+\sum_{n=1}^{\infty}f_n(x)t\exp\left(-n^2\pi^2\sigma t/x^2\right)\cos(n\pi z/x) \\
& +\sum_{n=1}^{\infty}g_n(x)z\exp\left(-n^2\pi^2\sigma t/x^2\right)\sin(n\pi z/x)+\sum_{m=2}^{\infty}a_m\cos(2m\pi t) \\
& +\sum_{n=1}^{\infty}\sum_{m=2}^{\infty}a_{nm}(x)\sin(2m\pi t)\cos(n\pi z/x)+\sum_{n=1}^{\infty}\sum_{m=2}^{\infty}b_{nm}(x)\cos(2m\pi t)\cos(n\pi z/x) \\
& +\sum_{n=1}^{\infty}\sum_{m=2}^{\infty}c_{nm}(x)z\cos(2m\pi t)\sin(n\pi z/x)+\sum_{n=1}^{\infty}\sum_{m=2}^{\infty}d_{nm}(x)z\sin(2m\pi t)\sin(n\pi z/x)
\end{aligned} \tag{A2}$$

where

$$a_0(x)=\frac{1}{c_k\pi}\left[F(x)\left(-\frac{1-e^{-x}}{x^2}+\frac{e^{-x}}{x}\right)\right]$$

$$b_0(x)=\frac{1}{2\pi x}\left(-\frac{F(x)}{x}\right)$$

$$c_0(x)=\frac{1}{2c_k}\left[\frac{2}{3}F(x)-\frac{F(x)}{x}\left(\frac{1-e^{-x}}{x}\right)+F(x)\left(\frac{e^{-x}}{x}\right)\right]$$

$$d_0(x)=\frac{1}{2c_k x}\left(-\frac{F(x)}{x}\right)$$

$$a_n(x) = \frac{2n^2\pi^2}{x^3\left(4\pi^2+{c_k}^2n^4\pi^4/x^4\right)}\left\{F(x)\pi\left[-\frac{(-1)^ne^{-x}}{1+n^2\pi^2/x^2}-\frac{2\left(1-(-1)^ne^{-x}\right)n^2\pi^2}{\left(1+n^2\pi^2/x^2\right)^2x^3}+\frac{4x}{n^2\pi^2}\right.\right.$$
$$\left.\left.-\frac{1}{x}\left(-\frac{1-(-1)^ne^{-x}}{1+n^2\pi^2/x^2}+\frac{2x^2}{n^2\pi^2}\right)\left(3-\frac{4{c_k}^2n^4\pi^4}{\left(4\pi^2+{c_k}^2n^4\pi^4/x^4\right)x^4}\right)\right]\right\}$$

$$b_n(x) = -\frac{4\pi^2}{c_kx\left(4\pi^2+{c_k}^2n^4\pi^4/x^4\right)}\left\{F(x)\left[-\frac{(-1)^ne^{-x}}{1+n^2\pi^2/x^2}-\frac{2\left(1-(-1)^ne^{-x}\right)n^2\pi^2}{\left(1+n^2\pi^2/x^2\right)^2x^3}+\frac{4x}{n^2\pi^2}\right.\right.$$
$$\left.\left.+\frac{1}{x}\left(-\frac{1-(-1)^ne^{-x}}{1+n^2\pi^2/x^2}+\frac{2x^2}{n^2\pi^2}\right)\left(\frac{4{c_k}^2n^4\pi^4}{\left(4\pi^2+{c_k}^2n^4\pi^4/x^4\right)x^4}-1\right)\right]\right\}$$

$$c_n(x) = \frac{2n^3\pi^4F(x)}{x^5(4\pi^2+{c_k}^2n^4\pi^4/x^4)}\left(-\frac{1-(-1)^ne^{-x}}{1+n^2\pi^2/x^2}+\frac{2x^2}{n^2\pi^2}\right)$$

$$d_n(x) = -\frac{4n\pi^3F(x)}{c_kx^3(4\pi^2+{c_k}^2n^4\pi^4/x^4)}\left(-\frac{1-(-1)^ne^{-x}}{1+n^2\pi^2/x^2}+\frac{2x^2}{n^2\pi^2}\right)$$

$$e_n(x) = -\frac{F(x)}{c_kx}\left\{\frac{2}{\pi}\left[-\frac{(-1)^ne^{-x}}{1+n^2\pi^2/x^2}-\frac{2\left(1-(-1)^ne^{-x}\right)n^2\pi^2}{\left(1+n^2\pi^2/x^2\right)^2x^3}+\frac{1}{x}\frac{1-(-1)^ne^{-x}}{1+n^2\pi^2/x^2}\right]\right.$$
$$+\left[-\frac{(-1)^ne^{-x}}{1+n^2\pi^2/x^2}-\frac{2\left(1-(-1)^ne^{-x}\right)n^2\pi^2}{\left(1+n^2\pi^2/x^2\right)^2x^3}+\frac{2x}{n^2\pi^2}+\frac{1}{x}\frac{1-(-1)^ne^{-x}}{1+n^2\pi^2/x^2}\right]\left(1-\frac{4\pi^2}{\left(4\pi^2+{c_k}^2n^4\pi^4/x^4\right)}\right)$$
$$\left.-\frac{16{c_k}^2n^4\pi^6}{x^5\left(4\pi^2+{c_k}^2n^4\pi^4/x^4\right)^2}\left(-\frac{1-(-1)^ne^{-x}}{1+n^2\pi^2/x^2}+\frac{2x^2}{n^2\pi^2}\right)\right\}$$
$$-\frac{1}{c_kx}\frac{dF(x)}{dx}\left\{\frac{2}{\pi}\left[-\frac{1-(-1)^ne^{-x}}{1+n^2\pi^2/x^2}\right]+\left[-\frac{1-(-1)^ne^{-x}}{1+n^2\pi^2/x^2}+\frac{2x^2}{n^2\pi^2}\right]\left[1-\frac{4\pi^2}{\left(4m^2\pi^2+{c_k}^2n^4\pi^4/x^4\right)}\right]\right\}$$
$$-\frac{4}{c_k\pi x}\sum_{m=2}^{\infty}\left\{\frac{\cos(m\pi/2)}{1-m^2}\left\{F(x)\left(-\frac{(-1)^ne^{-x}}{1+n^2\pi^2/x^2}-\frac{2\left(1-(-1)^ne^{-x}\right)n^2\pi^2}{\left(1+n^2\pi^2/x^2\right)^2x^3}+\frac{1}{x}\frac{1-(-1)^ne^{-x}}{1+n^2\pi^2/x^2}\right)\left(1-\frac{4m^2\pi^2}{\left(4\pi^2+{c_k}^2n^4\pi^4/x^4\right)}\right)\right.\right.$$
$$\left.\left.-\frac{16{c_k}^2m^2n^4\pi^6F(x)}{x^5\left(4\pi^2+{c_k}^2n^4\pi^4/x^4\right)^2}\left[-\frac{1-(-1)^ne^{-x}}{1+n^2\pi^2/x^2}\right]\right\}\right\}$$

$$f_n(x) = -\frac{2n^2\pi F(x)}{x^4}\left[2\left(-\frac{1-(-1)^ne^{-x}}{1+n^2\pi^2/x^2}\right)+\pi\left(-\frac{1-(-1)^ne^{-x}}{1+n^2\pi^2/x^2}+\frac{2x^2}{n^2\pi^2}\right)\left(1-\frac{4\pi^2}{\left(4\pi^2+{c_k}^2n^4\pi^4/x^4\right)}\right)\right]$$
$$-\frac{8n^2\pi F(x)}{x^4}\sum_{m=2}^{\infty}\frac{\cos(m\pi/2)}{1-m^2}\left(1-\frac{4m^2\pi^2}{\left(4m^2\pi^2+{c_k}^2n^4\pi^4/x^4\right)}\right)\left[-\frac{1-(-1)^ne^{-x}}{1+n^2\pi^2/x^2}\right]$$

$$g_n(x) = -\frac{nF(x)}{c_kx^3}\left[\pi\left(-\frac{1-(-1)^ne^{-x}}{1+n^2\pi^2/x^2}+\frac{2x^2}{n^2\pi^2}\right)\left(1-\frac{4\pi^2}{\left(4\pi^2+D^2n^4\pi^4/x^4\right)}\right)+2\left(-\frac{1-(-1)^ne^{-x}}{1+n^2\pi^2/x^2}\right)\right]$$
$$-\frac{4nF(x)}{c_kx^3}\sum_{m=2}^{\infty}\frac{\cos(m\pi/2)}{1-m^2}\left(-\frac{1-(-1)^ne^{-x}}{1+n^2\pi^2/x^2}\right)\left(1-\frac{4m^2\pi^2}{\left(4m^2\pi^2+D^2n^4\pi^4/x^4\right)}\right)$$

$$a_m(x) = \frac{1}{c_k}\frac{2}{\pi}\sum_{m=2}^{\infty}\left[\frac{\cos(m\pi/2)}{1-m^2}\right]\left[\left(\frac{1-e^{-x}}{x}\right)\left(-\frac{F(x)}{x}\right)+F(x)\left(\frac{e^{-x}}{x}\right)\right]$$

$$a_{mn}(x) = -\frac{8mn^2\pi^2}{\left(4m^2\pi^2+c_k^2n^4\pi^4/x^4\right)x^3}\sum_{m=2}^{\infty}\frac{\cos(m\pi/2)}{1-m^2}\left\{F(x)\left[-\left(-\frac{(-1)^ne^{-x}}{1+n^2\pi^2/x^2}-\frac{2\left(1-(-1)^ne^{-x}\right)n^2\pi^2}{\left(1+n^2\pi^2/x^2\right)^2x^3}\right)\right.\right.$$
$$\left.\left.+\frac{1}{x}\left(-\frac{1-(-1)^ne^{-x}}{1+n^2\pi^2/x^2}\right)\left(3-\frac{4c_k^2n^4\pi^4}{x^4\left(4\pi^2+c_k^2n^4\pi^4/x^4\right)}\right)\right]\right\}$$

$$b_{mn}(x) = -\frac{4}{c_kx}\left[\frac{4m^2\pi}{\left(4m^2\pi^2+c_k^2n^4\pi^4/x^4\right)}\right]\sum_{m=2}^{\infty}\frac{\cos(m\pi/2)}{1-m^2}\left\{F(x)\left[\left(-\frac{(-1)^ne^{-x}}{1+n^2\pi^2/x^2}-\frac{2\left(1-(-1)^ne^{-x}\right)n^2\pi^2}{\left(1+n^2\pi^2/x^2\right)^2x^3}\right)\right.\right.$$
$$\left.\left.+\frac{1}{x}\left(-\frac{1-(-1)^ne^{-x}}{1+n^2\pi^2/x^2}\right)\left(\frac{4c_k^2n^4\pi^4}{\left(4m^2\pi^2+c_k^2n^4\pi^4/x^4\right)x^4}-1\right)\right]\right\}$$

$$c_{mn}(x) = \frac{8mn^3\pi^3F(x)}{\left(4m^2\pi^2+c_k^2n^4\pi^4/x^4\right)x^5}\sum_{m=2}^{\infty}\frac{\cos(m\pi/2)}{1-m^2}\left[-\frac{1-(-1)^ne^{-x}}{1+n^2\pi^2/x^2}\right]$$

$$d_{mn}(x) = -\frac{16nm^2\pi^2F(x)}{c_k\left(4m^2\pi^2+c_k^2n^4\pi^4/x^4\right)x^3}\sum_{m=2}^{\infty}\frac{\cos(m\pi/2)}{1-m^2}\left[-\frac{1-(-1)^ne^{-x}}{1+n^2\pi^2/x^2}\right]$$

Appendix C. Solutions for the Zero-Order Stream Function

$$\begin{aligned}\psi^{(0)} = {} & a_0(x)\psi_1^{(0)} + b_0(x)\psi_2^{(0)} + c_0(x)\psi_3^{(0)} + d_0(x)\psi_4^{(0)} \\ & + \sum_{n=1}^{\infty} a_n(x)\psi_5^{(0)} + \sum_{n=1}^{\infty} b_n(x)\psi_6^{(0)} + \sum_{n=1}^{\infty} c_n(x)\psi_7^{(0)} + \sum_{n=1}^{\infty} d_n(x)\psi_8^{(0)} + \sum_{n=1}^{\infty} e_n(x)\psi_9^{(0)} + \sum_{n=1}^{\infty} f_n(x)\psi_{10}^{(0)} \\ & + \sum_{n=1}^{\infty} g_n(x)\psi_{11}^{(0)} + \sum_{m=2}^{\infty} a_m\psi_{12}^{(0)} + \sum_{n=1}^{\infty}\sum_{m=2}^{\infty} a_{nm}(x)\psi_{13}^{(0)} + \sum_{n=1}^{\infty}\sum_{m=2}^{\infty} b_{nm}(x)\psi_{14}^{(0)} \\ & + \sum_{n=1}^{\infty}\sum_{m=2}^{\infty} c_{nm}(x)\psi_{15}^{(0)} + \sum_{n=1}^{\infty}\sum_{m=2}^{\infty} d_{nm}(x)\psi_{16}^{(0)}\end{aligned} \tag{A3}$$

The functions of $\psi_1^{(0)}, \ldots, \psi_{16}^{(0)}$ are given by:

(1) $\psi_1^{(0)}$:

$$\begin{aligned}\psi_1^{(0)} = {} & n_v\left\{\frac{\sinh\left(z\sqrt{c_d/c_v}\right) - z\sqrt{c_d/c_v}\cosh\left(x\sqrt{c_d/c_v}\right)}{\sinh\left(x\sqrt{c_d/c_v}\right) - x\sqrt{c_d/c_v}\cosh\left(x\sqrt{c_d/c_v}\right)}\left\{\frac{x^2}{2c_v(c_d/c_v)} - \frac{1}{c_v(c_d/c_v)^2}\left[\cosh\left(x\sqrt{c_d/c_v}\right) - 1\right]\right\}\right. \\ & - \frac{x\sinh\left(z\sqrt{c_d/c_v}\right) - z\sinh\left(x\sqrt{c_d/c_v}\right)}{\sinh\left(x\sqrt{c_d/c_v}\right) - x\sqrt{c_d/c_v}\cosh\left(x\sqrt{c_d/c_v}\right)}\left\{\frac{x}{c_v(c_d/c_v)} - \frac{1}{c_v(c_d/c_v)^2}\sqrt{c_d/c_v}\sinh\left(x\sqrt{c_d/c_v}\right)\right\} \\ & \left. + \frac{1}{2}\frac{z^2}{c_v(c_d/c_v)} - \frac{\left[\cosh\left(z\sqrt{c_d/c_v}\right) - 1\right]}{c_v(c_d/c_v)^2}\right\} \\ & - \frac{2n_v x^3}{c_v}\sum_{n=1}^{\infty}\left\{\frac{1}{{\beta_n}^2\sin\beta_n}\left[(x\sin(\beta_n z/x) - z\sin\beta_n)\left(\cos\beta_n + (\cos\beta_n - 1)/{\beta_n}^2 - \frac{1}{2}\right)\right]\right. \\ & \left.\times\left\{\frac{\exp\left[-\left(c_v(\beta_n/x)^2 + c_d\right)t\right]}{({\beta_n}^2 + (c_d/c_v)x^2)}\right\}\right.\end{aligned}$$

where β_n is the non-zero positive roots of the equation $\sin\beta_n = \beta_n\cos\beta_n$. In the following equations, β_m has the same meaning as β_n.

(2) $\psi_2^{(0)}$:

$$\begin{aligned}{\psi_2}^{(0)} = {} & n_v\sin(2\pi t)\left\{\frac{\sinh\left(z\sqrt{c_d/c_v}\right) - z\sqrt{c_d/c_v}\cosh\left(x\sqrt{c_d/c_v}\right)}{\sinh\left(x\sqrt{c_d/c_v}\right) - x\sqrt{c_d/c_v}\cosh\left(x\sqrt{c_d/c_v}\right)}\left\{\frac{x^2}{2c_v(c_d/c_v)} - \frac{1}{c_v(c_d/c_v)^2}\left[\cosh\left(x\sqrt{c_d/c_v}\right) - 1\right]\right\}\right. \\ & - \frac{x\sinh\left(z\sqrt{c_d/c_v}\right) - z\sinh\left(x\sqrt{c_d/c_v}\right)}{\sinh\left(x\sqrt{c_d/c_v}\right) - x\sqrt{c_d/c_v}\cosh\left(x\sqrt{c_d/c_v}\right)}\left\{\frac{x}{c_v(c_d/c_v)} - \frac{1}{c_v(c_d/c_v)^2}\sqrt{c_d/c_v}\sinh\left(x\sqrt{c_d/c_v}\right)\right\} \\ & \left. + \frac{1}{2}\frac{z^2}{c_v(c_d/c_v)} - \frac{1}{c_v(c_d/c_v)^2}\left[\cosh\left(z\sqrt{c_d/c_v}\right) - 1\right]\right\} \\ & + \frac{2n_v x^3}{c_v}(2\pi)\sum_{n=1}^{\infty}\left\{\frac{1}{{\beta_n}^2({\beta_n}^2 + (c_d/c_v)x^2)\sin\beta_n}\left[(x\sin(\beta_n z/x) - z\sin\beta_n)\left(\cos\beta_n + (\cos\beta_n - 1)/{\beta_n}^2 - \frac{1}{2}\right)\right]\right. \\ & \left.\times\left\{\frac{\left[c_v(\beta_n/x)^2 + c_d\right]\exp\left[-\left(c_v(\beta_n/x)^2 + c_d\right)t\right] - \left[c_v(\beta_n/x)^2 + c_d\right]\cos(2\pi t) - 2\pi\sin(2\pi t)}{\left[c_v(\beta_n/x)^2 + c_d\right]^2 + 4\pi^2}\right\}\right.\end{aligned}$$

(3) $\psi_3^{(0)}$:

$$\begin{aligned}{\psi_3}^{(0)} = {} & n_v\cos(2\pi t)\left\{\frac{\sinh\left(z\sqrt{c_d/c_v}\right) - z\sqrt{c_d/c_v}\cosh\left(x\sqrt{c_d/c_v}\right)}{\sinh\left(x\sqrt{c_d/c_v}\right) - x\sqrt{c_d/c_v}\cosh\left(x\sqrt{c_d/c_v}\right)}\left\{\frac{x^2}{2c_v(c_d/c_v)} - \frac{1}{c_v(c_d/c_v)^2}\left[\cosh\left(x\sqrt{c_d/c_v}\right) - 1\right]\right\}\right. \\ & - \frac{x\sinh\left(z\sqrt{c_d/c_v}\right) - z\sinh\left(x\sqrt{c_d/c_v}\right)}{\sinh\left(x\sqrt{c_d/c_v}\right) - x\sqrt{c_d/c_v}\cosh\left(x\sqrt{c_d/c_v}\right)}\left\{\frac{x}{c_v(c_d/c_v)} - \frac{1}{c_v(c_d/c_v)^2}\sqrt{c_d/c_v}\sinh\left(x\sqrt{c_d/c_v}\right)\right\} \\ & \left. + \frac{1}{2}\frac{z^2}{c_v(c_d/c_v)} - \frac{1}{c_v(c_d/c_v)^2}\left[\cosh\left(z\sqrt{c_d/c_v}\right) - 1\right]\right\} \\ & - \frac{2n_v x^3}{c_v}\sum_{n=1}^{\infty}\left\{\frac{1}{{\beta_n}^2({\beta_n}^2 + (c_d/c_v)x^2)\sin\beta_n}\left[(x\sin(\beta_n z/x) - z\sin\beta_n)\left(\cos\beta_n + (\cos\beta_n - 1)/{\beta_n}^2 - \frac{1}{2}\right)\right]\right. \\ & \times\left\{\exp\left[-\left(c_v(\beta_n/x)^2 + c_d\right)t\right]\right. \\ & \left.\left. + 2\pi\frac{-2\pi\exp\left[-\left(c_v(\beta_n/x)^2 + c_d\right)t\right] - \left[c_v(\beta_n/x)^2 + c_d\right]\sin(2\pi t) + 2\pi\cos(2\pi t)}{\left[c_v(\beta_n/x)^2 + c_d\right]^2 + 4\pi^2}\right\}\right.\end{aligned}$$

(4) $\psi_4^{(0)}$:

$$\begin{aligned}
\psi_4{}^{(0)} = \; & n_v\cos(2\pi t)\left\{\frac{12z^2(c_d/c_v)-24\left[\cosh\left(z\sqrt{c_d/c_v}\right)-1\right]+z^4(c_d/c_v)^2}{12c_v(c_d/c_v)^3}\right.\\
& +\frac{\left[\sinh\left(z\sqrt{c_d/c_v}\right)-z\sqrt{c_d/c_v}\cosh\left(x\sqrt{c_d/c_v}\right)\right]}{\left[\sinh\left(x\sqrt{c_d/c_v}\right)-x\sqrt{c_d/c_v}\cosh\left(x\sqrt{c_d/c_v}\right)\right]}\times\left\{\frac{12x^2(c_d/c_v)-24\left[\cosh\left(x\sqrt{c_d/c_v}\right)-1\right]+x^4(c_d/c_v)^2}{12c_v(c_d/c_v)^3}\right\}\\
& \left.+\frac{\left[x\sinh\left(z\sqrt{c_d/c_v}\right)-z\sinh\left(x\sqrt{c_d/c_v}\right)\right]}{\left[\sinh\left(x\sqrt{c_d/c_v}\right)-x\sqrt{c_d/c_v}\cosh\left(x\sqrt{c_d/c_v}\right)\right]}\times\left\{\frac{6\sqrt{c_d/c_v}\left[\sinh\left(x\sqrt{c_d/c_v}\right)-x\sqrt{c_d/c_v}\right]-x^3(c_d/c_v)^2}{3c_v(c_d/c_v)^3}\right\}\right\}\\
& -\frac{2n_vx^5}{c_v}\sum_{n=1}^{\infty}\frac{1}{\beta_n^6\sin\beta_n\left[1+c_dx^2/\left(c_v\beta_n^2\right)\right]}\left[x\sin(\beta_nz/x)-z\sin\beta_n\right]\left(1-\beta_n^2/4-2\cos\beta_n-2(\cos\beta_n-1)/\beta_n^2\right)\\
& \times\left\{\exp\left[-\left(c_v\beta_n^2/x^2+c_d\right)t\right]-2\pi\frac{2\pi\exp\left[-\left(c_v\beta_n^2/x^2+c_d\right)t\right]-2\pi\cos(2\pi t)+\left(c_v\beta_n^2/x^2+c_d\right)\sin(2\pi t)}{\left(c_v\beta_n^2/x^2+c_d\right)^2+4\pi^2}\right\}
\end{aligned}$$

(5) $\psi_5^{(0)}$:

$$\begin{aligned}
\psi_5{}^{(0)} = \; & n_v\left\{\frac{\left[1-\cosh\left(x\sqrt{c_d/c_v}\right)\right]\left[\sinh\left(z\sqrt{c_d/c_v}\right)-z\sqrt{c_d/c_v}\cosh\left(x\sqrt{c_d/c_v}\right)\right]}{c_v(c_d/c_v)\left(c_d/c_v+\frac{n^2\pi^2}{x^2}\right)\left[\sinh\left(x\sqrt{c_d/c_v}\right)-x\sqrt{c_d/c_v}\cosh\left(x\sqrt{c_d/c_v}\right)\right]}\right.\\
& +\frac{\left[1-\cosh\left(z\sqrt{c_d/c_v}\right)\right]}{c_v(c_d/c_v)\left(c_d/c_v+\frac{n^2\pi^2}{x^2}\right)}+\frac{\sinh\left(x\sqrt{c_d/c_v}\right)\left[x\sinh\left(z\sqrt{c_d/c_v}\right)-z\sinh\left(x\sqrt{c_d/c_v}\right)\right]}{c_v\sqrt{c_d/c_v}\left(c_d/c_v+\frac{n^2\pi^2}{x^2}\right)\left[\sinh\left(x\sqrt{c_d/c_v}\right)-x\sqrt{c_d/c_v}\cosh\left(x\sqrt{c_d/c_v}\right)\right]}\\
& \left.+\frac{x^2}{n^2\pi^2}\frac{[1-\cos(n\pi z/x)]}{c_v\left(c_d/c_v+\frac{n^2\pi^2}{x^2}\right)}+\frac{x^2}{n^2\pi^2}\frac{\left[1-(-1)^n\right]\left[\sinh\left(z\sqrt{c_d/c_v}\right)-z\sqrt{c_d/c_v}\cosh\left(x\sqrt{c_d/c_v}\right)\right]}{c_v\left(c_d/c_v+\frac{n^2\pi^2}{x^2}\right)\left[\sinh\left(x\sqrt{c_d/c_v}\right)-x\sqrt{c_d/c_v}\cosh\left(x\sqrt{c_d/c_v}\right)\right]}\right\}\sin(2\pi t)\\
& +(2\pi)\frac{2x^3n_v}{n^2\pi^2}\sum_{m=1}^{\infty}\frac{[x\sin(\beta_mz/x)-z\sin\beta_m]}{(c_v{\beta_m}^2+c_dx^2)(n^2\pi^2-{\beta_m}^2)\sin\beta_m}\left\{\left[1-(-1)^n\right]-\frac{n^2\pi^2}{{\beta_m}^2}(1-\cos\beta_m)+\frac{n^2\pi^2}{\beta_m}\sin\beta_m\right\}\\
& \times\frac{-\left(c_v(\beta_m/x)^2+c_d\right)\exp\left[-\left(c_v(\beta_m/x)^2+c_d\right)t\right]+\left(c_v(\beta_m/x)^2+c_d\right)\cos(2\pi t)+2\pi\sin(2\pi t)}{\left[c_v(\beta_m/x)^2+c_d\right]^2+4\pi^2}
\end{aligned}$$

(6) $\psi_6^{(0)}$:

$$\begin{aligned}
\psi_6{}^{(0)} = \; & n_v\cos(2\pi t)\left\{\frac{\left[1-\cosh\left(x\sqrt{c_d/c_v}\right)\right]\left[\sinh\left(z\sqrt{c_d/c_v}\right)-z\sqrt{c_d/c_v}\cosh\left(x\sqrt{c_d/c_v}\right)\right]}{c_v(c_d/c_v)\left(c_d/c_v+\frac{n^2\pi^2}{x^2}\right)\left[\sinh\left(x\sqrt{c_d/c_v}\right)-x\sqrt{c_d/c_v}\cosh\left(x\sqrt{c_d/c_v}\right)\right]}\right.\\
& +\frac{\left[1-\cosh\left(z\sqrt{c_d/c_v}\right)\right]}{c_v(c_d/c_v)\left(c_d/c_v+\frac{n^2\pi^2}{x^2}\right)}+\frac{\sinh\left(x\sqrt{c_d/c_v}\right)\left[x\sinh\left(z\sqrt{c_d/c_v}\right)-z\sinh\left(x\sqrt{c_d/c_v}\right)\right]}{c_v\sqrt{c_d/c_v}\left(c_d/c_v+\frac{n^2\pi^2}{x^2}\right)\left[\sinh\left(x\sqrt{c_d/c_v}\right)-x\sqrt{c_d/c_v}\cosh\left(x\sqrt{c_d/c_v}\right)\right]}\\
& \left.+\frac{x^2}{n^2\pi^2}\frac{[1-\cos(n\pi z/x)]}{c_v\left(c_d/c_v+\frac{n^2\pi^2}{x^2}\right)}+\frac{x^2}{n^2\pi^2}\frac{\left[1-(-1)^n\right]\left[\sinh\left(z\sqrt{c_d/c_v}\right)-z\sqrt{c_d/c_v}\cosh\left(x\sqrt{c_d/c_v}\right)\right]}{c_v\left(c_d/c_v+\frac{n^2\pi^2}{x^2}\right)\left[\sinh\left(x\sqrt{c_d/c_v}\right)-x\sqrt{c_d/c_v}\cosh\left(x\sqrt{c_d/c_v}\right)\right]}\right\}\\
& +\frac{2x^3n_v}{n^2\pi^2}\sum_{m=1}^{\infty}\frac{[x\sin(\beta_mz/x)-z\sin\beta_m]}{(c_v{\beta_m}^2+c_dx^2)(n^2\pi^2-{\beta_m}^2)\sin\beta_m}\left\{\left[1-(-1)^n\right]-\frac{n^2\pi^2}{{\beta_m}^2}(1-\cos\beta_m)+\frac{n^2\pi^2}{\beta_m}\sin\beta_m\right\}\\
& \times\left\{\exp\left[-\left(c_v(\beta_m/x)^2+c_d\right)t\right]-(2\pi)\frac{2\pi\exp\left[-\left(c_v(\beta_m/x)^2+c_d\right)t\right]-2\pi\cos(2\pi t)+\left[c_v(\beta_m/x)^2+c_d\right]\sin(2\pi t)}{\left[c_v(\beta_m/x)^2+c_d\right]^2+4\pi^2}\right\}
\end{aligned}$$

(7) $\psi_7^{(0)}$:

$$\begin{aligned}
\psi_7{}^{(0)} = \; & \frac{n_v\sin(2\pi t)}{\left(c_d+\frac{c_vn^2\pi^2}{x^2}\right)^2}\left\{\left\{\frac{2x}{n\pi}\left(2c_v+c_dx^2/n^2\pi^2\right)\left[1-(-1)^n\right]+\frac{2{c_v}^2n\pi}{c_dx}\left[1-\cosh\left(x\sqrt{c_d/c_v}\right)\right]\right\}\right.\\
& \times\left[\frac{\sinh\left(z\sqrt{c_d/c_v}\right)-z\sqrt{c_d/c_v}\cosh\left(x\sqrt{c_d/c_v}\right)}{\sinh\left(x\sqrt{c_d/c_v}\right)-x\sqrt{c_d/c_v}\cosh\left(x\sqrt{c_d/c_v}\right)}\right]\\
& +\frac{\sin(2\pi t)}{\left(c_d+\frac{c_vn^2\pi^2}{x^2}\right)}\frac{x^2}{n^2\pi^2}\left\{n\pi(-1)^n+\frac{2{c_v}^{3/2}\sinh\left(x\sqrt{c_d/c_v}\right)}{\sqrt{c_d}\left(c_d+c_v\frac{n^2\pi^2}{x^2}\right)}\frac{n^3\pi^3}{x^3}\right\}\times\left[\frac{x\sinh\left(z\sqrt{c_d/c_v}\right)-z\sinh\left(x\sqrt{c_d/c_v}\right)}{\sinh\left(x\sqrt{c_d/c_v}\right)-x\sqrt{c_d/c_v}\cosh\left(x\sqrt{c_d/c_v}\right)}\right]\\
& \left.+\frac{c_v\sin(2\pi t)}{\left(c_d+\frac{c_vn^2\pi^2}{x^2}\right)^2}\left\{\frac{2x}{n\pi}[1-\cos(n\pi z/x)]\left(2+\frac{c_d}{c_v}\frac{x^2}{n^2\pi^2}\right)-z\sin(n\pi z/x)\left(1+\frac{c_d}{c_v}\frac{x^2}{n^2\pi^2}\right)+\frac{2c_vn\pi\left[1-\cosh\left(z\sqrt{c_d/c_v}\right)\right]}{c_dx}\right\}\right\}\\
& -\frac{2c_vn_v(2\pi)}{x^3}\sum_{m=1}^{\infty}\frac{1}{\sin\beta_m}[x\sin(\beta_mz/x)-z\sin\beta_m]\left[F_{7nm}|_{z=-x}+x\frac{\partial F_{7nm}}{\partial z}\Big|_{z=-x}\right]
\end{aligned}$$

where

$$F_{7nm}|_{z=-x} + x\left.\frac{\partial F_{7nm}}{\partial z}\right|_{z=-x}$$
$$= \left(-\frac{x^4}{c_k}\right)\left(\frac{x^2}{n^2\pi^2}\right)\frac{1}{(n^2\pi^2-\beta_m{}^2)(-c_v\beta_m{}^2-c_dx^2)}\frac{-\left(c_v(\beta_m/x)^2+c_d\right)\exp\left(-\left(c_v(\beta_m/x)^2+c_d\right)t\right)+\left(c_v(\beta_m/x)^2+c_d\right)\cos(2\pi t)+2\pi\sin(2\pi t)}{\left[c_v(\beta_m/x)^2+c_d\right]^2+4\pi^2}\times$$
$$\left\{\frac{2x^2\left(2n^2\pi^2-\beta_m{}^2\right)}{n\pi(n^2\pi^2-\beta_m{}^2)}\left[(-1)^n-1\right]-n\pi x(-1)^n-\frac{2x^4}{\beta_m}\left(\frac{n\pi}{x}\right)^3\frac{\sin\beta_m}{(n^2\pi^2-\beta_m{}^2)}-\frac{2x^5}{\beta_m{}^2}\left(\frac{n\pi}{x}\right)^3\frac{1}{\left(n^2\pi^2-\beta_m^2\right)}(\cos\beta_m-1)\right\}$$

(8) $\psi_8^{(0)}$:

$$\begin{aligned}\psi_8{}^{(0)} = {} & \frac{n_v\cos(2\pi t)}{\left(c_d+c_v\frac{n^2\pi^2}{x^2}\right)^2}\left\{\left\{\frac{2x}{n\pi}\left(2c_v+c_dx^2/n^2\pi^2\right)\left[1-(-1)^n\right]+\frac{2c_v{}^2n\pi}{c_dx}\left[1-\cosh\left(x\sqrt{c_d/c_v}\right)\right]\right\}\right.\\
& \times\left[\frac{\sinh\left(z\sqrt{c_d/c_v}\right)-z\sqrt{c_d/c_v}\cosh\left(x\sqrt{c_d/c_v}\right)}{\sinh\left(x\sqrt{c_d/c_v}\right)-x\sqrt{c_d/c_v}\cosh\left(x\sqrt{c_d/c_v}\right)}\right]\\
& +\frac{\cos(2\pi t)}{\left(c_d+c_v\frac{n^2\pi^2}{x^2}\right)}\frac{x^2}{n^2\pi^2}\left\{n\pi(-1)^n+\frac{2c_v{}^{3/2}\sinh\left(x\sqrt{c_d/c_v}\right)}{\sqrt{c_d}\left(c_d+c_v\frac{n^2\pi^2}{x^2}\right)}\frac{n^3\pi^3}{x^3}\right\}\times\left[\frac{x\sinh\left(z\sqrt{c_d/c_v}\right)-z\sinh\left(x\sqrt{c_d/c_v}\right)}{\sinh\left(x\sqrt{c_d/c_v}\right)-x\sqrt{c_d/c_v}\cosh\left(x\sqrt{c_d/c_v}\right)}\right]\\
& \left.+\frac{c_v}{\left(c_d+\frac{c_vn^2\pi^2}{x^2}\right)^2}\left\{\frac{2x}{n\pi}[1-\cos(n\pi z/x)]\left(2+\frac{c_d}{c_v}\frac{x^2}{n^2\pi^2}\right)-z\sin(n\pi z/x)\left(1+\frac{c_d}{c_v}\frac{x^2}{n^2\pi^2}\right)+\frac{2c_vn\pi\left[1-\cosh\left(z\sqrt{c_d/c_v}\right)\right]}{c_dx}\right\}\right\}\\
& -\frac{2n_vc_v}{x^3}\sum_{m=1}^{\infty}\frac{1}{\sin\beta_m}[x\sin(\beta_mz/x)-z\sin\beta_m]\left[F_{8nm}|_{z=-x}+x\left.\frac{\partial F_{8nm}}{\partial z}\right|_{z=-x}\right]\end{aligned}$$

where

$$F_{8nm}|_{z=-x} + x\left.\frac{\partial F_{8nm}}{\partial z}\right|_{z=-x}$$
$$= \left(-\frac{x^4}{c_k}\right)\left(\frac{x^2}{n^2\pi^2}\right)\frac{1}{(n^2\pi^2-\beta_m{}^2)(-c_v\beta_m{}^2-c_dx^2)}\left[\exp\left(-\left(c_v(\beta_m/x)^2+c_d\right)t\right)-(2\pi)\frac{2\pi\exp\left(-\left(c_v(\beta_m/x)^2+c_d\right)t\right)-2\pi\cos(2\pi t)+\left[c_v(\beta_m/x)^2+c_d\right]\sin(2\pi t)}{\left[c_v(\beta_m/x)^2+c_d\right]^2+4\pi^2}\right]\times$$
$$\left\{\frac{2x^2\left(2n^2\pi^2-\beta_m{}^2\right)}{n\pi(n^2\pi^2-\beta_m{}^2)}\left[(-1)^n-1\right]-n\pi x(-1)^n-\frac{2x^4}{\beta_m}\left(\frac{n\pi}{x}\right)^3\frac{\sin\beta_m}{(n^2\pi^2-\beta_m{}^2)}-\frac{2x^5}{\beta_m{}^2}\left(\frac{n\pi}{x}\right)^3\frac{1}{\left(n^2\pi^2-\beta_m^2\right)}(\cos\beta_m-1)\right\}$$

(9) $\psi_9^{(0)}$:

$$\begin{aligned}\psi_9{}^{(0)} = {} & \frac{n_v\left[\sinh\left(z\sqrt{(-c_kn^2\pi^2/x^2+c_d)/c_v}\right)-z\sqrt{(-c_kn^2\pi^2/x^2+c_d)/c_v}\cosh\left(x\sqrt{(-c_kn^2\pi^2/x^2+c_d)/c_v}\right)\right]}{\left[\sinh\left(x\sqrt{(-c_kn^2\pi^2/x^2+c_d)/c_v}\right)-x\sqrt{(-c_kn^2\pi^2/x^2+c_d)/c_v}\cosh\left(x\sqrt{(-c_kn^2\pi^2/x^2+c_d)/c_v}\right)\right]}F_{9n0}|_{z=-x}\\
& +\frac{n_v\left[x\sinh\left(z\sqrt{(-c_kn^2\pi^2/x^2+c_d)/c_v}\right)-z\sinh\left(x\sqrt{(-c_kn^2\pi^2/x^2+c_d)/c_v}\right)\right]}{\left[\sinh\left(x\sqrt{(-c_kn^2\pi^2/x^2+c_d)/c_v}\right)-x\sqrt{(-c_kn^2\pi^2/x^2+c_d)/c_v}\cosh\left(x\sqrt{(-c_kn^2\pi^2/x^2+c_d)/c_v}\right)\right]}\left.\frac{\partial F_{9n0}}{\partial z}\right|_{z=-x}\\
& +n_vF_{9n0}+\frac{2n_vc_v}{x^3}\sum_{m=1}^{\infty}\frac{1}{\sin\beta_m}[x\sin(\beta_mz/x)-z\sin\beta_m]\left(F_{9nm}|_{z=-x}+x\left.\frac{\partial F_{9nm}}{\partial z}\right|_{z=-x}\right)\end{aligned}$$

where

$$F_{9n0} = -\frac{1}{c_v-c_k+c_dx^2/(n\pi)^2}\left(\frac{x}{n\pi}\right)^4\left\{[\cos(n\pi z/x)-1]-\frac{c_v}{\left(c_k-c_dx^2/(n\pi)^2\right)}\left[\cosh\left(z\sqrt{(-n^2\pi^2c_k/x^2+c_d)/c_v}\right)-1\right]\right\}\times\exp\left[-(n\pi/x)^2c_kt\right]$$

$$F_{9nm}|_{z=-x} + x\left.\frac{\partial F_{9nm}}{\partial z}\right|_{z=-x} = \frac{x^4}{c_v}\left(\frac{x}{n\pi}\right)^2\frac{\exp\left[-\left(c_v(\beta_m/x)^2+c_d\right)t\right]}{(n^2\pi^2-\beta_m{}^2)(c_kn^2\pi^2-c_v\beta_m{}^2-c_dx^2)}\times\left\{\left[(-1)^n-1\right]-\frac{n^2\pi^2}{\beta_m{}^2}(\cos\beta_m-1)-n^2\pi^2\cos\beta_m\right\}$$

(10) $\psi_{10}^{(0)}$:

$$\begin{aligned}\psi_{10}{}^{(0)} = {} & \frac{n_v\left[\sinh\left(z\sqrt{(-c_kn^2\pi^2/x^2+c_d)/c_v}\right)-z\sqrt{(-c_kn^2\pi^2/x^2+c_d)/c_v}\cosh\left(x\sqrt{(-c_kn^2\pi^2/x^2+c_d)/c_v}\right)\right]}{\left[\sinh\left(x\sqrt{(-c_kn^2\pi^2/x^2+c_d)/c_v}\right)-x\sqrt{(-c_kn^2\pi^2/x^2+c_d)/c_v}\cosh\left(x\sqrt{(-c_kn^2\pi^2/x^2+c_d)/c_v}\right)\right]}F_{10n0}|_{z=-x}\\
& +\frac{n_v\left[x\sinh\left(z\sqrt{(-c_kn^2\pi^2/x^2+c_d)/c_v}\right)-z\sinh\left(x\sqrt{(-c_kn^2\pi^2/x^2+c_d)/c_v}\right)\right]}{\left[\sinh\left(x\sqrt{(-c_kn^2\pi^2/x^2+c_d)/c_v}\right)-x\sqrt{(-c_kn^2\pi^2/x^2+c_d)/c_v}\cosh\left(x\sqrt{(-c_kn^2\pi^2/x^2+c_d)/c_v}\right)\right]}\left.\frac{\partial F_{10n0}}{\partial z}\right|_{z=-x}\\
& +n_vF_{10n0}+\frac{2n_vc_v}{x^3}\sum_{m=1}^{\infty}\frac{1}{\sin\beta_m}[x\sin(\beta_mz/x)-z\sin\beta_m]\left[F_{10nm}|_{z=-x}+x\left.\frac{\partial F_{10nm}}{\partial z}\right|_{z=-x}\right]\end{aligned}$$

where

$$F_{10n0} = -\frac{1}{c_v - c_k + c_d x^2/(n\pi)^2}\left(\frac{x}{n\pi}\right)^4\left\{[\cos(n\pi z/x) - 1] - \frac{c_v}{\left(c_k - c_d x^2/(n\pi)^2\right)}\left[\cosh\left(z\sqrt{\frac{-n^2\pi^2 c_k/x^2 + c_d}{c_v}}\right) - 1\right]\right\} \times t\exp\left[-(n\pi/x)^2 c_k t\right]$$

$$F_{10nm}|_{z=-x} + x\frac{\partial F_{10nm}}{\partial z}\Big|_{z=-x} = \frac{x^6}{c_v}\left(\frac{x}{n\pi}\right)^2 \frac{\exp\left[-\left(c_v(\beta_m/x)^2 + c_d\right)t\right] - \exp\left[-c_k(n\pi/x)^2 t\right]}{(n^2\pi^2 - {\beta_m}^2)(c_k n^2\pi^2 - c_v{\beta_m}^2 - c_d x^2)} \times \left\{\left[(-1)^n - 1\right] - \frac{n^2\pi^2}{{\beta_m}^2}(\cos\beta_m - 1) - n^2\pi^2\cos\beta_m\right\}$$

(11) $\psi_{11}^{(0)}$:

$$\begin{aligned}
\psi_{11}^{(0)} = \; & n_v \frac{\sinh\left(z\sqrt{(-c_k n^2\pi^2/x^2 + c_d)/c_v}\right) - z\sqrt{(-c_k n^2\pi^2/x^2 + c_d)/c_v}\cosh\left(x\sqrt{(-c_k n^2\pi^2/x^2 + c_d)/c_v}\right)}{\sinh\left(x\sqrt{(-c_k n^2\pi^2/x^2 + c_d)/c_v}\right) - x\sqrt{(-c_k n^2\pi^2/x^2 + c_d)/c_v}\cosh\left(x\sqrt{(-c_k n^2\pi^2/x^2 + c_d)/c_v}\right)} F_{11n0}|_{z=-x} \\
& + \frac{n_v x\sinh\left(z\sqrt{(-c_k n^2\pi^2/x^2 + c_d)/c_v}\right) - z\sinh\left(x\sqrt{(-c_k n^2\pi^2/x^2 + c_d)/c_v}\right)}{\sinh\left(x\sqrt{(-c_k n^2\pi^2/x^2 + c_d)/c_v}\right) - x\sqrt{(-c_k n^2\pi^2/x^2 + c_d)/c_v}\cosh\left(x\sqrt{(-c_k n^2\pi^2/x^2 + c_d)/c_v}\right)} \frac{\partial F_{11n0}}{\partial z}\Big|_{z=-x} \\
& - \frac{n_v}{\left(c_v + c_d\frac{x^2}{n^2\pi^2} - c_k\right)}\left(\frac{x^4}{n^4\pi^4}\right) \times \exp\left[-c_k(n\pi/x)^2 t\right] \\
& \times \left\{\frac{2x}{n\pi}\frac{2c_v - \left(c_k - c_d x^2/n^2\pi^2\right)}{\left(c_v + c_d\frac{x^2}{n^2\pi^2} - c_k\right)}[\cos(n\pi z/x) - 1] + z\sin(n\pi z/x) - \frac{2{c_v}^2}{\left(c_v + c_d\frac{x^2}{n^2\pi^2} - c_k\right)(c_k - c_d x^2/n^2\pi^2)}\left(\frac{x}{n\pi}\right)\left[\cosh\left(z\sqrt{\frac{-c_k n^2\pi^2/x^2 + c_d}{c_v}}\right) - 1\right]\right\} \\
& + \frac{2n_v c_v}{x^3}\sum_{m=1}^{\infty}\frac{1}{\sin\beta_m}[x\sin(\beta_m z/x) - z\sin\beta_m]\left(F_{11nm}|_{z=-x} + x\frac{\partial F_{11nm}}{\partial z}\Big|_{z=-x}\right)
\end{aligned}$$

where

$$\begin{aligned}
F_{11n0} = \; & -\frac{1}{\left(c_v + c_d\frac{x^2}{n^2\pi^2} - c_k\right)}\left(\frac{x^4}{n^4\pi^4}\right) \times \exp\left[-c_k(n\pi/x)^2 t\right] \\
& \times \left\{\frac{2x}{n\pi}\frac{2c_v - \left(c_k - c_d x^2/n^2\pi^2\right)}{\left(c_v + c_d\frac{x^2}{n^2\pi^2} - c_k\right)}[\cos(n\pi z/x) - 1] + z\sin(n\pi z/x) - \frac{2{c_v}^2}{\left(c_v + c_d\frac{x^2}{n^2\pi^2} - c_k\right)(c_k - c_d x^2/n^2\pi^2)}\left(\frac{x}{n\pi}\right)\left[\cosh\left(z\sqrt{\frac{-c_k n^2\pi^2/x^2 + c_d}{c_v}}\right) - 1\right]\right\}
\end{aligned}$$

$$\begin{aligned}
& F_{11nm}|_{z=-x} + x\frac{\partial F_{11nm}}{\partial z}\Big|_{z=-x} \\
& = \left(-\frac{x^4}{c_v}\right)\left(\frac{x^2}{n^2\pi^2}\right)\frac{\exp\left(-\left(c_v(\beta_m/x)^2 + c_d\right)t\right)}{(n^2\pi^2 - {\beta_m}^2)(c_k n^2\pi^2 - c_v{\beta_m}^2 - c_d x^2)} \times \\
& \left\{\frac{2x^2\left(2n^2\pi^2 - {\beta_m}^2\right)}{n\pi(n^2\pi^2 - {\beta_m}^2)}\left[(-1)^n - 1\right] - n\pi x(-1)^n - \frac{2x^4}{\beta_m}\left(\frac{n\pi}{x}\right)^3\frac{\sin\beta_m}{(n^2\pi^2 - {\beta_m}^2)} - \frac{2x^5}{{\beta_m}^2}\left(\frac{n\pi}{x}\right)^3\frac{1}{(n^2\pi^2 - {\beta_m}^2)}(\cos\beta_m - 1)\right\}
\end{aligned}$$

(12) $\psi_{12}^{(0)}$:

$$\begin{aligned}
\psi_{12}^{(0)}(x,z,t) = \; & n_v\cos(2m\pi t)\left\{\frac{\sinh\left(z\sqrt{c_d/c_v}\right) - z\sqrt{c_d/c_v}\cosh\left(x\sqrt{c_d/c_v}\right)}{\sinh\left(x\sqrt{c_d/c_v}\right) - x\sqrt{c_d/c_v}\cosh\left(x\sqrt{c_d/c_v}\right)}\left\{\frac{x^2}{2c_v(c_d/c_v)} - \frac{1}{c_v(c_d/c_v)^2}\left[\cosh\left(x\sqrt{c_d/c_v}\right) - 1\right]\right\}\right. \\
& - \frac{x\sinh\left(z\sqrt{c_d/c_v}\right) - z\sinh\left(x\sqrt{c_d/c_v}\right)}{\sinh\left(x\sqrt{c_d/c_v}\right) - x\sqrt{c_d/c_v}\cosh\left(x\sqrt{c_d/c_v}\right)}\left\{\frac{x}{c_v(c_d/c_v)} - \frac{1}{c_v(c_d/c_v)^2}\sqrt{c_d/c_v}\sinh\left(x\sqrt{c_d/c_v}\right)\right\} \\
& \left. + \frac{1}{2}\frac{z^2}{c_v(c_d/c_v)} - \frac{1}{c_v(c_d/c_v)^2}\left[\cosh\left(z\sqrt{c_d/c_v}\right) - 1\right]\right\} \\
& - \frac{2n_v x^3}{c_v}\sum_{n=1}^{\infty}\left\{\frac{1}{{\beta_n}^2({\beta_n}^2 + (c_d/c_v)x^2)\sin\beta_n}\left[(x\sin(\beta_n z/x) - z\sin\beta_n)\left(\cos\beta_n + (\cos\beta_n - 1)/{\beta_n}^2 - \frac{1}{2}\right)\right]\right. \\
& \times \left\{\exp\left[-\left(c_v(\beta_n/x)^2 + c_d\right)t\right]\right. \\
& \left.\left. + 2m\pi\frac{-2m\pi\exp\left[-\left(c_v(\beta_n/x)^2 + c_d\right)t\right] - \left[c_v(\beta_n/x)^2 + c_d\right]\sin(2m\pi t) + 2m\pi\cos(2m\pi t)}{\left[c_v(\beta_n/x)^2 + c_d\right]^2 + 4m^2\pi^2}\right\}\right\}
\end{aligned}$$

(13) $\psi_{13}^{(0)}$:

$$\begin{aligned}\psi_{13}^{(0)} = \; & n_v\left\{\frac{\left[1-\cosh\left(x\sqrt{c_d/c_v}\right)\right]\left[\sinh\left(z\sqrt{c_d/c_v}\right)-z\sqrt{c_d/c_v}\cosh\left(x\sqrt{c_d/c_v}\right)\right]}{c_v(c_d/c_v)\left(\frac{c_d}{c_v}+\frac{n^2\pi^2}{x^2}\right)\left[\sinh\left(x\sqrt{c_d/c_v}\right)-x\sqrt{c_d/c_v}\cosh\left(x\sqrt{c_d/c_v}\right)\right]}\right.\\ & +\frac{\left[1-\cosh\left(z\sqrt{c_d/c_v}\right)\right]}{c_v(c_d/c_v)\left(\frac{c_d}{c_v}+\frac{n^2\pi^2}{x^2}\right)}+\frac{\sinh\left(x\sqrt{c_d/c_v}\right)\left[x\sinh\left(z\sqrt{c_d/c_v}\right)-z\sinh\left(x\sqrt{c_d/c_v}\right)\right]}{c_v\sqrt{(c_d/c_v)}\left(\frac{c_d}{c_v}+\frac{n^2\pi^2}{x^2}\right)\left[\sinh\left(x\sqrt{c_d/c_v}\right)-x\sqrt{c_d/c_v}\cosh\left(x\sqrt{c_d/c_v}\right)\right]}\\ & \left.+\frac{x^2}{n^2\pi^2}\frac{[1-\cos(n\pi z/x)]}{c_v\left(\frac{c_d}{c_v}+\frac{n^2\pi^2}{x^2}\right)}+\frac{x^2}{n^2\pi^2}\frac{\left[1-(-1)^n\right]\left[\sinh\left(z\sqrt{c_d/c_v}\right)-z\sqrt{c_d/c_v}\cosh\left(x\sqrt{c_d/c_v}\right)\right]}{c_v\left(\frac{c_d}{c_v}+\frac{n^2\pi^2}{x^2}\right)\left[\sinh\left(x\sqrt{c_d/c_v}\right)-x\sqrt{c_d/c_v}\cosh\left(x\sqrt{c_d/c_v}\right)\right]}\right\}\sin(2m\pi t)\\ & +(2m\pi)\frac{2x^3n_v}{n^2\pi^2}\sum_{m=1}^{\infty}\frac{[x\sin(\beta_m z/x)-z\sin\beta_m]}{(c_v{\beta_m}^2+c_d x^2)(n^2\pi^2-{\beta_m}^2)\sin\beta_m}\left\{\left[1-(-1)^n\right]-\frac{n^2\pi^2}{{\beta_m}^2}(1-\cos\beta_m)+\frac{n^2\pi^2}{\beta_m}\sin\beta_m\right\}\\ & \times\frac{-\left(c_v(\beta_m/x)^2+c_d\right)\exp\left[-\left(c_v(\beta_m/x)^2+c_d\right)t\right]+\left(c_v(\beta_m/x)^2+c_d\right)\cos(2m\pi t)+2m\pi\sin(2m\pi t)}{\left[c_v(\beta_m/x)^2+c_d\right]^2+4m^2\pi^2}\end{aligned}$$

(14) $\psi_{14}^{(0)}$:

$$\begin{aligned}\psi_{14}^{(0)} = \; & \cos(2m\pi t)\left\{\frac{n_v\left[1-\cosh\left(x\sqrt{c_d/c_v}\right)\right]\left[\sinh\left(z\sqrt{c_d/c_v}\right)-z\sqrt{c_d/c_v}\cosh\left(x\sqrt{c_d/c_v}\right)\right]}{c_v\left(\frac{c_d}{c_v}\right)\left(\frac{c_d}{c_v}+\frac{n^2\pi^2}{x^2}\right)\left[\sinh\left(x\sqrt{c_d/c_v}\right)-x\sqrt{c_d/c_v}\cosh\left(x\sqrt{c_d/c_v}\right)\right]}\right.\\ & +\frac{n_v\left[1-\cosh\left(z\sqrt{c_d/c_v}\right)\right]}{c_v(c_d/c_v)\left(\frac{c_d}{c_v}+\frac{n^2\pi^2}{x^2}\right)}+\frac{n_v\sinh\left(x\sqrt{c_d/c_v}\right)\left[x\sinh\left(z\sqrt{c_d/c_v}\right)-z\sinh\left(x\sqrt{c_d/c_v}\right)\right]}{c_v\sqrt{(c_d/c_v)}\left(\frac{c_d}{c_v}+\frac{n^2\pi^2}{x^2}\right)\left[\sinh\left(x\sqrt{c_d/c_v}\right)-x\sqrt{c_d/c_v}\cosh\left(x\sqrt{c_d/c_v}\right)\right]}\\ & \left.+\frac{x^2}{n^2\pi^2}\frac{n_v[1-\cos(n\pi z/x)]}{c_v\left(\frac{c_d}{c_v}+\frac{n^2\pi^2}{x^2}\right)}+\frac{x^2}{n^2\pi^2}\frac{n_v\left[1-(-1)^n\right]\left[\sinh\left(z\sqrt{c_d/c_v}\right)-z\sqrt{c_d/c_v}\cosh\left(x\sqrt{c_d/c_v}\right)\right]}{c_v\left(\frac{c_d}{c_v}+\frac{n^2\pi^2}{x^2}\right)\left[\sinh\left(x\sqrt{c_d/c_v}\right)-x\sqrt{c_d/c_v}\cosh\left(x\sqrt{c_d/c_v}\right)\right]}\right\}\\ & +\frac{2x^3n_v}{n^2\pi^2}\sum_{m=1}^{\infty}\frac{[x\sin(\beta_m z/x)-z\sin\beta_m]}{(c_v{\beta_m}^2+c_d x^2)(n^2\pi^2-{\beta_m}^2)\sin\beta_m}\left\{\left[1-(-1)^n\right]-\frac{n^2\pi^2}{{\beta_m}^2}(1-\cos\beta_m)+\frac{n^2\pi^2}{\beta_m}\sin\beta_m\right\}\\ & \times\left\{\exp\left[-\left(c_v(\beta_m/x)^2+c_d\right)t\right]-(2m\pi)\frac{2m\pi\exp\left[-\left(c_v(\beta_m/x)^2+c_d\right)t\right]-2m\pi\cos(2m\pi t)+\left[c_v(\beta_m/x)^2+c_d\right]\sin(2m\pi t)}{\left[c_v(\beta_m/x)^2+c_d\right]^2+4m^2\pi^2}\right\}\end{aligned}$$

(15) $\psi_{15}^{(0)}$:

$$\begin{aligned}\psi_{15}^{(0)} = \; & \frac{n_v\sin(2m\pi t)}{\left(c_d+c_v\frac{n^2\pi^2}{x^2}\right)^2}\left\{\left\{\frac{2x}{n\pi}\left(2c_v+c_d x^2/n^2\pi^2\right)\left[1-(-1)^n\right]+\frac{2{c_v}^2n\pi}{c_d x}\left[1-\cosh\left(x\sqrt{c_d/c_v}\right)\right]\right\}\right.\\ & \times\left[\frac{\sinh\left(z\sqrt{c_d/c_v}\right)-z\sqrt{c_d/c_v}\cosh\left(x\sqrt{c_d/c_v}\right)}{\sinh\left(x\sqrt{c_d/c_v}\right)-x\sqrt{c_d/c_v}\cosh\left(x\sqrt{c_d/c_v}\right)}\right]\\ & +\frac{\sin(2m\pi t)}{\left(c_d+c_v\frac{n^2\pi^2}{x^2}\right)}\frac{x^2}{n^2\pi^2}\left\{n\pi(-1)^n+\frac{2{c_v}^{3/2}\sinh\left(x\sqrt{c_d/c_v}\right)}{\sqrt{c_d}\left(c_d+c_v\frac{n^2\pi^2}{x^2}\right)}\frac{n^3\pi^3}{x^3}\right\}\times\left[\frac{x\sinh\left(z\sqrt{c_d/c_v}\right)-z\sinh\left(x\sqrt{c_d/c_v}\right)}{\sinh\left(x\sqrt{c_d/c_v}\right)-x\sqrt{c_d/c_v}\cosh\left(x\sqrt{c_d/c_v}\right)}\right]\\ & \left.+\frac{c_v\sin(2m\pi t)}{\left(c_d+\frac{c_v n^2\pi^2}{x^2}\right)^2}\left\{\frac{2x}{n\pi}[1-\cos(n\pi z/x)]\left(2+\frac{c_d}{c_v}\frac{x^2}{n^2\pi^2}\right)-z\sin(n\pi z/x)\left(1+\frac{c_d}{c_v}\frac{x^2}{n^2\pi^2}\right)+\frac{2c_v n\pi\left[1-\cosh\left(z\sqrt{c_d/c_v}\right)\right]}{c_d x}\right\}\right\}\\ & -\frac{2c_v n_v(2m\pi)}{x^3}\sum_{m=1}^{\infty}\frac{1}{\sin\beta_m}[x\sin(\beta_m z/x)-z\sin\beta_m]\left[F_{15nm}|_{z=-x}+x\frac{\partial F_{15nm}}{\partial z}\Big|_{z=-x}\right]\end{aligned}$$

where

$$\begin{aligned}& F_{15nm}|_{z=-x}+x\frac{\partial F_{15nm}}{\partial z}\Big|_{z=-x}\\ & =\left(-\frac{x^4}{c_k}\right)\left(\frac{x^2}{n^2\pi^2}\right)\frac{1}{(n^2\pi^2-{\beta_m}^2)(-c_v{\beta_m}^2-c_d x^2)}\frac{-\left(c_v(\beta_m/x)^2+c_d\right)\exp\left(-\left(c_v(\beta_m/x)^2+c_d\right)t\right)+\left(c_v(\beta_m/x)^2+c_d\right)\cos(2m\pi t)+2m\pi\sin(2m\pi t)}{\left[c_v(\beta_m/x)^2+c_d\right]^2+4m^2\pi^2}\times\\ & \left\{\frac{2x^2\left(2n^2\pi^2-{\beta_m}^2\right)}{n\pi(n^2\pi^2-{\beta_m}^2)}\left[(-1)^n-1\right]-n\pi x(-1)^n-\frac{2x^4}{\beta_m}\left(\frac{n\pi}{x}\right)^3\frac{\sin\beta_m}{(n^2\pi^2-{\beta_m}^2)}-\frac{2x^5}{{\beta_m}^2}\left(\frac{n\pi}{x}\right)^3\frac{1}{\left(n^2\pi^2-\beta_m^2\right)}(\cos\beta_m-1)\right\}\end{aligned}$$

(16) $\psi_{16}^{(0)}$:

$$
\begin{aligned}
\psi_{16}^{(0)} = \; & \frac{n_v \cos(2m\pi t)}{\left(c_d + c_v \frac{n^2\pi^2}{x^2}\right)^2} \left\{ \frac{2x}{n\pi} \left(2c_v + c_d x^2/n^2\pi^2\right) \left[1 - (-1)^n\right] + \frac{2{c_v}^2 n\pi}{c_d x} \left[1 - \cosh\left(x\sqrt{c_d/c_v}\right)\right] \right\} \\
& \times \left[\frac{\sinh\left(z\sqrt{c_d/c_v}\right) - z\sqrt{c_d/c_v}\cosh\left(x\sqrt{c_d/c_v}\right)}{\sinh\left(x\sqrt{c_d/c_v}\right) - x\sqrt{c_d/c_v}\cosh\left(x\sqrt{c_d/c_v}\right)} \right] \\
& + \frac{n_v \cos(2m\pi t)}{\left(c_d + c_v \frac{n^2\pi^2}{x^2}\right)} \frac{x^2}{n^2\pi^2} \left\{ n\pi(-1)^n + \frac{2{c_v}^{3/2}\sinh\left(x\sqrt{c_d/c_v}\right)}{\sqrt{c_d}\left(c_d + c_v \frac{n^2\pi^2}{x^2}\right)} \frac{n^3\pi^3}{x^3} \right\} \times \left[\frac{x\sinh\left(z\sqrt{c_d/c_v}\right) - z\sinh\left(x\sqrt{c_d/c_v}\right)}{\sinh\left(x\sqrt{c_d/c_v}\right) - x\sqrt{c_d/c_v}\cosh\left(x\sqrt{c_d/c_v}\right)} \right] \\
& + \frac{c_v n_v \cos(2m\pi t)}{\left(c_d + \frac{c_v n^2\pi^2}{x^2}\right)^2} \left\{ \frac{2x}{n\pi} \left[1 - \cos(n\pi z/x)\right] \left(2 + \frac{c_d}{c_v} \frac{x^2}{n^2\pi^2}\right) - z\sin(n\pi z/x) \left(1 + \frac{c_d}{c_v} \frac{x^2}{n^2\pi^2}\right) + \frac{2c_v n\pi \left[1 - \cosh\left(z\sqrt{c_d/c_v}\right)\right]}{c_d x} \right\} \\
& - \frac{2n_v c_v}{x^3} \sum_{m=1}^{\infty} \frac{1}{\sin\beta_m} \left[x\sin(\beta_m z/x) - z\sin\beta_m\right] \left[F_{16nm}|_{z=-x} + x \frac{\partial F_{16nm}}{\partial z}\Big|_{z=-x} \right]
\end{aligned}
$$

where

$$
\begin{aligned}
& F_{16nm}|_{z=-x} + x \frac{\partial F_{16nm}}{\partial z}\Big|_{z=-x} \\
& = \left(-\frac{x^4}{c_k}\right) \left(\frac{x^2}{n^2\pi^2}\right) \frac{1}{(n^2\pi^2 - \beta_m{}^2)(-c_v\beta_m{}^2 - c_d x^2)} \left[\exp\left(-\left(c_v(\beta_m/x)^2 + c_d\right)t\right) - (2m\pi) \frac{2m\pi\exp\left(-\left(c_v(\beta_m/x)^2 + c_d\right)t\right) - 2m\pi\cos(2m\pi t) + \left[c_v(\beta_m/x)^2 + c_d\right]\sin(2m\pi t)}{\left[c_v(\beta_m/x)^2 + c_d\right]^2 + 4m^2\pi^2} \right] \\
& \times \left\{ \frac{2x^2\left(2n^2\pi^2 - \beta_m{}^2\right)}{n\pi(n^2\pi^2 - \beta_m{}^2)} \left[(-1)^n - 1\right] - n\pi x(-1)^n - \frac{2x^4}{\beta_m} \left(\frac{n\pi}{x}\right)^3 \frac{\sin\beta_m}{(n^2\pi^2 - \beta_m{}^2)} - \frac{2x^5}{\beta_m{}^2} \left(\frac{n\pi}{x}\right)^3 \frac{1}{\left(n^2\pi^2 - \beta_m^2\right)} (\cos\beta_m - 1) \right\}
\end{aligned}
$$

References

1. James, W.F.; Barko, J.W. Estimation of phosphorous exchange between littoral and pelagic zones during nighttime convection circulation. *Limnol. Oceanogr.* **1991**, *36*, 179–187. [CrossRef]
2. MacIntyre, S.; Melack, J.M. Vertical and horizontal transport in lakes: Linking moral, benthic, and pelagic habitats. *J. N Am. Benthol. Soc.* **1995**, *14*, 599–615. [CrossRef]
3. Huai, W.X.; Zeng, Y.H.; Xu, Z.G.; Yang, Z.H. Three-layer model for vertical velocity distribution in open channel flow with submerged rigid vegetation. *Adv. Water Resour.* **2009**, *32*, 487–492. [CrossRef]
4. Lin, Y.-T. Wind effect on diurnal thermally driven flow in vegetated nearshore of a lake. *Environ. Fluid Mech.* **2015**, *15*, 161–178. [CrossRef]
5. Ho, H.C.; Lin, Y.T. Gravity currents over a rigid and emergent vegetated slope. *Adv. Water Resour.* **2015**, *76*, 72–80. [CrossRef]
6. Kirk, J.T.O. *Light and Photosynthesis in Aquatic Ecosystem*, 3rd ed.; Cambridge University Press: Cambridge, MA, USA, 2011.
7. Zhang, X.; Nepf, H.M. Thermally driven exchange flow between open water and an aquatic canopy. *J. Fluid Mech.* **2009**, *632*, 227–243. [CrossRef]
8. Lin, Y.-T.; Ye, Y.-Q.; Han, D.-R.; Chiu, Y.-J. Propagation and Separation of Downslope Gravity Currents over Rigid and Emergent Vegetation Patches in Linearly Stratified Environments. *J. Mar. Sci. Eng.* **2022**, *10*, 308. [CrossRef]
9. Monismith, S.B.; Imberger, J.; Morison, M.L. Convective motion in the sidearm of a small reservoir. *Limnol. Oceanogr.* **1990**, *35*, 1676–1702. [CrossRef]
10. Farrow, D.E.; Patterson, J.C. On the response of a reservoir sidearm to diurnal heating and cooling. *J. Fluid Mech.* **1993**, *246*, 143–161. [CrossRef]
11. Coates, M.; Ferris, J. The radiatively driven natural convection beneath a floating plant layer. *Limnol. Oceanogr.* **1994**, *39*, 1186–1194.
12. Zhang, X.; Nepf, H.M. Density driven exchange flow between open water and an aquatic canopy. *Water Resour. Res.* **2008**, *44*, W08417. [CrossRef]
13. Horsh, G.M.; Stefan, H.G. Convective circulation in littoral water due to surface cooling. *Limnol. Oceanogr.* **1988**, *33*, 1068–1083. [CrossRef]
14. Farrow, D.E. Periodically forced natural convection over slowly varying topography. *J. Fluid Mech.* **2004**, *508*, 1–21. [CrossRef]
15. Lövstedt, C.; Bengtsson, L. Density-driven current between reed belts and open water in a shallow lake. *Water Resour. Res.* **2008**, *44*, W10413. [CrossRef]
16. Adams, E.E.; Wells, S.A. Field measurements on side arms of Lake Anna. *J. Hydraul Engng* **1984**, *110*, 773–793. [CrossRef]
17. Farrow, D.E.; Patterson, J.C. The daytime circulation and temperature pattern in a reservoir sidearm. *Int. J. Heat Mass Transf.* **1994**, *37*, 1957–1968. [CrossRef]
18. Lei, C.; Patterson, J.C. Unsteady natural convection in a triangular enclosure induced by absorption of radiation. *J. Fluid Mech.* **2002**, *460*, 181–209. [CrossRef]
19. Lei, C.; Patterson, J.C. Unsteady natural convection in a triangular enclosure induced by surface cooling. *Int. J. Heat Fluid Flow* **2005**, *26*, 307–321. [CrossRef]
20. Drazin, P.G.; Reid, W.H. *Hydrodynamic Stability*, 2nd ed.; Cambridge University Press: Cambridge, UK, 2004.
21. Lei, C.; Patterson, J.C. Natural convection induced by diurnal heating and cooling in a reservoir with slowly varying topography. *JSME Int. J. Ser. B Fluids Therm. Eng.* **2006**, *49*, 605–615. [CrossRef]

22. Bednarz, T.P.; Lei, C.; Patterson, J.C. Unsteady natural convection induced by diurnal temperature changes in a reservoir with slowly varying bottom topography. *Int. J. Ther. Sci.* **2009**, *48*, 1932–1942. [CrossRef]
23. Oldham, C.E.; Sturman, J.J. The effect of emergent vegetation on convective flushing in shallow wetlands: Scaling and experiment. *Limnol. Oceanogr.* **2001**, *46*, 1486–1493. [CrossRef]
24. Tanino, Y.; Nepf, H.M.; Kulis, P.S. Gravity current in aquatic canopies. *Water Resour. Res.* **2005**, *41*, W12402. [CrossRef]
25. Lin, Y.-T.; Wu, C.H. The role of rooted emergent vegetation on periodically thermal-driven flow over a sloping bottom. *Environ. Fluid Mech.* **2014**, *14*, 1303–1334. [CrossRef]
26. Lin, Y.-T.; Wu, C.H. Effects of a sharp change of emergent vegetation distributions on thermally driven flow over a slope. *Environ. Fluid Mech.* **2015**, *15*, 771–791. [CrossRef]
27. Pokorny, J.; Kvet, J. Aquatic plants and lake ecosystem. *Lakes Handb.* **2004**, *1*, 309–340.
28. Jamali, M.; Zhang, X.; Nepf, H.M. Exchange flow between a canopy and open water. *J. Fluid Mech.* **2008**, *611*, 237–254. [CrossRef]
29. Poulikakos, D.; Bejan, A. The fluid dynamics of an attic space. *J. Fluid Mech.* **1983**, *131*, 251–269. [CrossRef]
30. Farrow, D.E. Unsteady Natural Convection in Reservoir Sidearms. Ph.D. Thesis, University of Western Australia, Crawley, Australia, 1991.
31. Kays, W.M. Turbulent Prandtle Number-where are we? *J. Heat Transf.* **1994**, *166*, 284–295. [CrossRef]
32. Sturman, J.J.; Oldham, C.E.; Ivey, G.N. Steady convection exchange flow down slopes. *Aquat Sci* **1999**, *61*, 260–278. [CrossRef]